Research Square

Preprints are preliminary reports that have not undergone peer review.
They should not be considered conclusive, used to inform clinical practice,
or referenced by the media as validated information.

Impact of Wire Harness Inductance on Hall Effect Thruster Discharge Oscillations

Ajay Krishnan

ajaykrishnan@gatech.edu

Georgia Institute of Technology

Daniel Troyetsky

Stanford University

Dan Lev

Georgia Institute of Technology

Kentaro Hara

Stanford University

Mitchell Walker

Georgia Institute of Technology

Maryam Saeedifard

Georgia Institute of Technology

Research Article

Keywords:

Posted Date: September 16th, 2026

DOI: https://doi.org/10.21203/rs.3.rs-10857813/v1

License: This work is licensed under a Creative Commons Attribution 4.0 International License.
Read Full License

Additional Declarations: No competing interests reported.

Impact of Wire Harness Inductance on Hall Effect Thruster Discharge Oscillations

Ajay Krishnan*, Dan Lev†, Mitchell Walker‡ and Maryam Saeedifard§
Georgia Institute of Technology, Atlanta, Georgia, 30332, USA

Daniel Troyetsky¶, Kentaro Hara‖
Stanford University, Stanford, California, 94305, USA

I. Abstract

The wire harness is a critical component of the Hall effect thruster (HET) discharge circuit. Its length, and therefore its inductance, can vary between ground tests and spaceflight, leading to differences in discharge oscillations. While the simplest approach would be to minimize harness length by positioning the electrical filter close to the thruster, this may not always be feasible. In this work, we investigate the influence of harness inductance on oscillations of a H6 HET in discharge voltage, discharge current, cathode-to-ground and thruster-to-ground potentials, power supply current, and plasma parameters using a variable inductor over a range of inductances from 16.6 µH to 104.6 µH at two operating voltages of 300 V and 400 V. We find that the root mean square (RMS) discharge voltage increases linearly with harness inductance at an operating voltage of 300 V, but exhibits nonlinear behavior and is more oscillatory at 400 V, based on mean normalized analysis. At 300 V, the RMS discharge current peaks at 0.33 A (approximately 6% of the mean discharge current) at 39.6 μH, whereas at 400 V, the RMS discharge current reaches a minimum of 0.7 A (approximately 14% of the mean discharge current) at 44.6 μH.

To further interpret these results, we apply an extended Kalman filter coupled to a zero-dimensional plasma model, yielding time-resolved estimates of ion and neutral number densities, electron temperature, electron axial bulk velocity, and electron cross-field mobility as a function of harness inductance. The analysis shows that heavy species dynamics track the main discharge current oscillation, i.e., the breathing mode, while the electron dynamics contain high-frequency components in the GHz range. Furthermore, the normalized RMS oscillation of cross-field electron mobility increases with harness inductance, matching discharge voltage behavior at 300 V and both voltage and current at 400 V. In particular, the electron mobility increases from a peak value of 13.3 m^2/Vs at 16.6 μH to 13.4 m^2/Vs at 104.6 μH at 300 V. At 400 V, the electron mobility decreases from 2.75×10^8 $1/s$ at 16.6 μH to a minimum of 2.675×10^8 $1/s$ at 34.6 μH, to a maximum of 2.775×10^8 $1/s$ at 94.6 μH. These findings inform thruster and power system integration strategies by highlighting the role of series inductance in shaping discharge oscillations and pointing toward design approaches such as reactive compensation, power factor correction, and impedance matching for maximum power transfer.

II. Nomenclature

V	=	Voltage	I	=	Current
ID	=	Discharge Current	Z	=	Impedance

*Graduate Research Assistant, School of Electrical and Computer Engineering, ajaykrishnan@gatech.edu
†Research Engineer, School of Aerospace Engineering, dan.lev@gatech.edu
‡Chair, School of Aerospace Engineering, mitchell.walker@coe.gatech.edu
§Professor, School of Electrical and Computer Engineering, maryam@ece.gatech.edu
¶PhD Candidate, Department of Aeronautics and Astronautics, dtroyets@stanford.edu
‖Associate Professor, Department of Aeronautics and Astronautics, kenhara@stanford.edu

VD	=	Discharge Voltage
VCG	=	Cathode-to-Ground Voltage
R	=	Resistance
C	=	Capacitance
CP	=	Power Supply Capacitance
RHP	=	Power Supply Harness Resistance
CHP	=	Power Supply Harness Capacitance
CF	=	Filter Capacitance
LF	=	Filter Inductance
LHT	=	Thruster Harness Inductance
HPEPL	=	High-Power Electric Propulsion Laboratory
PPU	=	Power Processing Unit
VTF	=	Vacuum Test Facility
BM	=	Breathing Mode
PID	=	Proportional-Integral-Derivative
AC	=	Alternating Current
RMS	=	Root Mean Square
K_P	=	Proportional Gain
KCL	=	Kirchhoff's Current Law
IPS	=	Power Supply Current
VTBG	=	Thruster Body-to-Ground Voltage
L	=	Inductance
VP	=	Power Supply Voltage
VP	=	Power Supply Voltage
LHP	=	Power Supply Harness Inductance
RF	=	Filter Resistance
RHT	=	Thruster Harness Resistance
	=	
CHT	=	Thruster Harness Capacitance
ODE	=	Ordinary Differential Equation
HET	=	Hall Effect Thruster
MFC	=	Mass Flow Controller
FFT	=	Fast Fourier Transform
DC	=	Direct Current
K_D	=	Derivative Gain
PP	=	Peak-to-Peak
K_I	=	Integral Gain
	=	

III. Introduction

A Hall effect thruster (HET) is a plasma device that generates thrust via the electrostatic acceleration of ions [1, 2]. First developed in the 1960s, HETs have been increasingly used as a propulsion option for satellites due to their mass savings as compared to chemical propulsion devices [2]. To increase their usage in satellites and deep space missions, it is critical to advance HET technology by increasing thrust, specific impulse, efficiency, and lifetime. The development of HET technology requires operating HETs in ground-based vacuum facilities while replicating the conditions of the space environment. However, it is not possible to fully emulate space conditions on the ground, leading to unintended deviation in thruster behavior as measured in space [3].

Vacuum chambers introduce "facility effects" that change thruster performance and thruster plume and discharge physics on the ground compared to space [3–6]. Some facility effects occur because ground facility pumping systems cannot reach the low-pressure levels that exist in space [7]. In addition, the existence of a large conductive chamber walls creates current paths that otherwise do not exist in the space environment [3–6]. Lastly, sputtering emanating from the chamber walls back onto and into the thruster may interfere with the HET discharge and affect lifetime [3]. Thus, it is critical to understand the influence of various facility-related factors on HET physics and operation and to be able to correctly determine space performance based on ground testing.

Discharge current oscillations are the result of plasma instabilities in a HET discharge [8, 9]. Of the various HET oscillation types, the predominant type is the so-called breathing mode (BM) oscillation that is tied to predator-prey interactions between electrons and neutrals in the discharge plasma [10, 11]. They present plasma parameter variations, specifically plasma density, in the discharge chamber of the HET. BM oscillatory dynamics can be expressed through the conservation of mass, momentum, and energy equations and can be used to define the discharge plasma as an electrical load [12]. This dominant mode occurs in the tens of kHz range and can lead to discharge current amplitudes greater than 100% of the mean [10]. The mode plays a significant role in the dynamics and performance of a HET, as highly oscillatory thrusters exhibit reduced lifetimes [2].

Data collected from space missions have revealed performance disparities between space and ground conditions [3]. The electrical harness, a vital component of the discharge circuit, has different lengths and thus inductances that differ between ground-based development testing and operation on the spacecraft. Harnesses, which are transmission lines, are defined by a forward path, the anode line, and a return path, the cathode line, to transmit power from source

to load. Any harnessing that may exist between the PPU and the discharge filter is referred to as the power supply harness, whereas any harnessing between the discharge filter and the HET is referred to as the thruster harness, as shown in Figure 1. Harnesses can be made of copper wire or even other materials such as silver. American Wire Gauge 6 electrical harness, which is commonly used in HET circuits, typically has a resistance, inductance, and capacitance per unit meter of roughly 3 mOhm/m, 0.4 µH/m and 59 pF/m, respectively [13–15].

The discharge voltage and current oscillations could contribute to HET erosion at high amplitudes. To address this issue, it is generally recommended to minimize the harness length and inductance by relocating the filter close to the thruster. While relocating the filter holds the potential to increase harness inductance and subsequently decrease system complexity and costs, it is important to note that this physical configuration may not always be feasible. Alternative options to mitigate inductance include employing engineering techniques like busbars, which are thick metal strips used for distributing current, although this approach may present challenges, particularly in the context of spacecraft applications [13].

Past work on harness analysis was performed Pinero *et al.* at the NASA Glenn Research Center and by Brieda *et al.* [13, 14]. Pinero focused on an experimental approach while Brieda focused on a simulation-based approach. Pinero used a breakout box with changeable components to vary the inductance of the harness. Both studies determined that voltage oscillations scale linearly with inductance, but with further increases in inductance, Brieda shows that voltage oscillations begin to decrease. The decrease in voltage oscillations might be due to nonlinear effects between the harness inductance and the discharge plasma, where current oscillations are reduced, leading to reduced voltage oscillations. However, Brieda's computational results have not been verified experimentally. It is thus important to experimentally determine the effects of higher inductance levels. Higher inductances could, in fact, reduce oscillations due to nonlinear impedance interactions with the HET load.

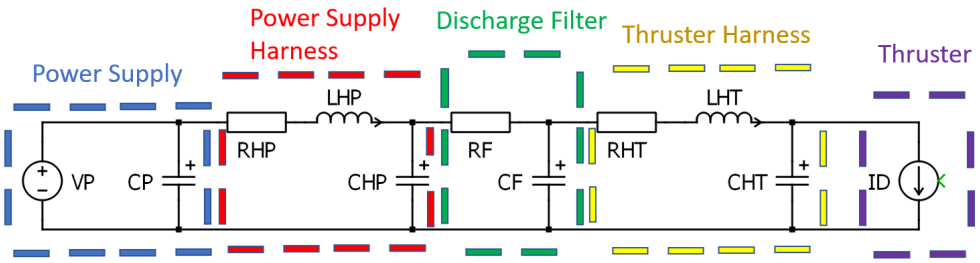


Fig. 1 Discharge Circuit Diagram of an Electric Propulsion System

In this paper, we aim to understand the effects of harness inductance on HET discharge electrical parameters. We also seek to study the coupling between the electrical and plasma parameters of the HET discharge plasma using a state estimation framework. The paper is broken down into the following sections: Section IV discusses the electrical circuit concepts relevant to the harness discussion. Section V outlines the methods used to conduct the harness experiment. Section VI discusses the results obtained from the harness experiment. Section VII explores the coupling between the discharge circuit and the discharge plasma. Lastly, Section VIII provides conclusions for the harness experiment.

IV. Electrical Circuit Background

In this section, we discuss the electrical circuit background needed to better understand the objectives of the harness experiment. We start by discussing frequency domain representations of the electrical harness, which informs the reader what equivalent circuit is sufficient to account for BM oscillations. We then discuss the lumped and distributed harness models, which given the reader insight into what models can be constructed for a given harness. We then introduce the concept of real, reactive, and apparent power from breathing mode oscillations, along with maximum power transfer and the reflection coefficient, which explain how harness inductance and impedance can interact with the HET load to alter BM oscillations. We introduce how inductance plays a damping role in the discharge circuit by presenting a relation derived using KCL that relates the discharge current and several RLC filter parameters. We finish by discussing ignition characteristics of HETs, which together with BM oscillations describe the two parts of HET operation where harness inductance is relevant.

Figure 2 shows the impedance magnitude, $|Z|$, as a function of frequency for the lumped electrical wire thruster

harness RLC model from Figure 1 for a 64 meter long harness. The complex impedance of a lumped RLC network is given by

$$Z(\omega) = \frac{R + j\omega L}{1 - \omega^2 LC + j\omega RC}. \tag{1}$$

Here, the resistance is 0.179 Ohms in the initial flat region from 1 Hz to 1 kHz, as resistance does not vary with frequency, the inductance is 25.6 μH in the subsequent positive slope region from 1 kHz to 250 kHz, and lastly the capacitance is 3.776 nF in the negative slope region from 750 kHz to 10 MHz. A resonant peak exists at 500 kHz. In a HET, the breathing mode frequency is in the tens of kilohertz range and thus lies within the inductive region of the impedance magnitude as a function of frequency plot. Thus, the harness can be modeled as an inductor, with some small resistance while the capacitance can be neglected.

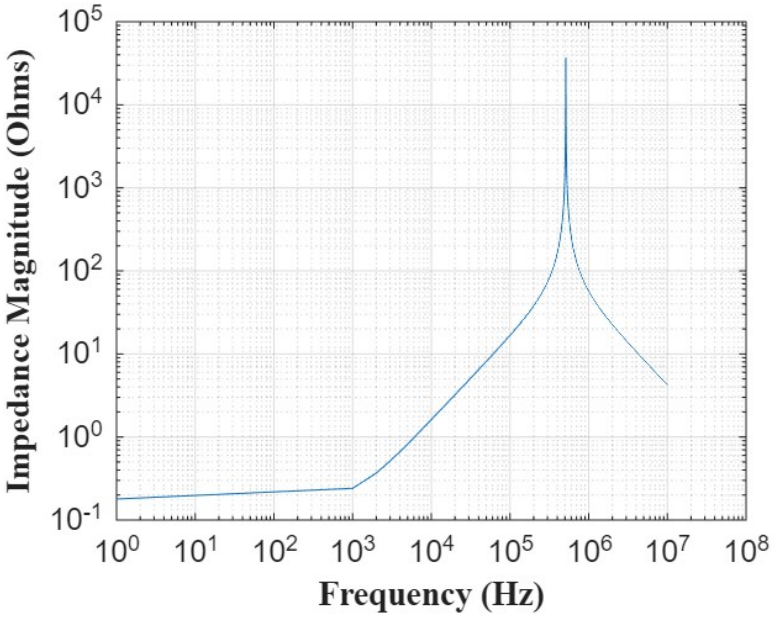


Fig. 2 Harness Impedance Magnitude as a Function of Frequency

The differences in inductance result in differences in the voltage oscillations of HET [13]. Due to the discharge filter, oscillatory current does not flow through the power supply harness and does not significantly contribute to discharge voltage oscillations, thus we can often ignore it. In the thruster harness, CHT is often very small and negligible on the order of nanofarads, leaving RHT and LHT as the most significant sources of oscillations. The origin of the voltage oscillation comes from the time-varying discharge current that flows through the inductor, as shown by $V = L\frac{dI}{dt}$.

Figure 3 and Figure 4 show impedance data obtained from the 64 meter long Gauge 6 harness, as measured from the discharge filter to the thruster and back with the power supply harness and power supply disconnected, in the High-Power Electric Propulsion Laboratory (HPEPL) using a Keysight E4990A impedance analyzer with an impedance measurement uncertainty of ±0.045%. The anode and cathode lines were shorted together, with no plasma being present. The impedance analyzer applies a test voltage over a sweep of frequency, measures the current response, and computes the impedance as their quotient. It can be observed from Figure 3 that the impedance magnitude-frequency plot transitions from resistive to inductive at approximately 500 Hz and from inductive to capacitive at approximately 400 kHz, but then suddenly changes in behavior to inductive with another resonant peak at 500 kHz. Several more LC resonant peaks can be observed as frequency increases, specifically at 600 kHz, 800 kHz, 1 MHz, 2.5 MHz, 3.5 MHz, 4.5 MHz, 6 MHz, and 9.5 MHz. This suggests that the harness equivalent RLC model consists of more than the configuration shown in Figure 1. The harness would likely have to be modeled by several stages of RLC components to capture high frequency effects above 500 kHz.

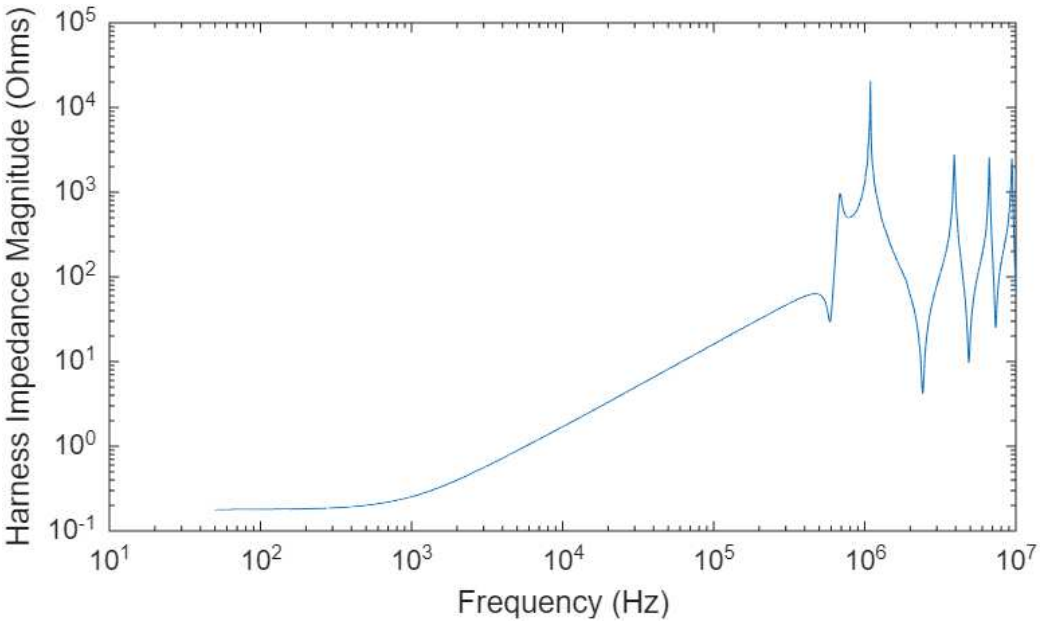


Fig. 3 HPEPL Harness Impedance Magnitude as a Function of Frequency

Figure 4 shows how the phase changes as a function of frequency. Positive phase shifts indicate that the voltage is leading the current, whereas negative phase shifts indicate that the voltage is lagging the current. Inductors have the voltage leading the current by 90 degrees, while capacitors have the voltage lagging behind the current by 90 degrees. These effects can be observed in the inductive region from 1 kHz to 500 kHz where the phase is 90 degrees, and at frequencies 1 MHz and above where the phase shifts between 90 degrees and -90 degrees.

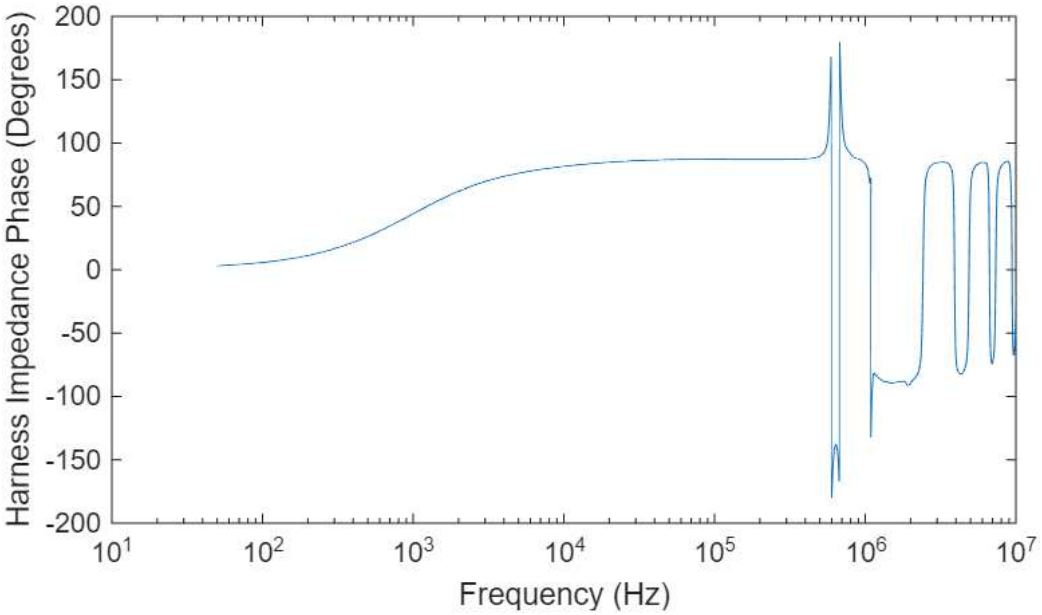


Fig. 4 HPEPL Harness Impedance Phase as a Function of Frequency

The circuit analysis performed on a transmission line depends on its wavelength, which represents the physical distance the electromagnetic wave or signal propagates during one cycle, computed using $c = \lambda f$, where c is the speed of light, λ is the wavelength, and f is the frequency of the wave. If the length of the transmission line is less than the wavelength of the wave, then the circuit model is lumped. If it is greater, then the model is distributed, as shown

in Figure 5, which involves several cascaded RLC stages where the transmission line is described by a PDE. In the VTF-2 setup at HPEPL, since the harness is approximately 64 m in length, the circuit model can be taken to be lumped for frequencies up to 4.5 MHz after which the wavelength exceeds the physical length of the harness and results in a distributed model.

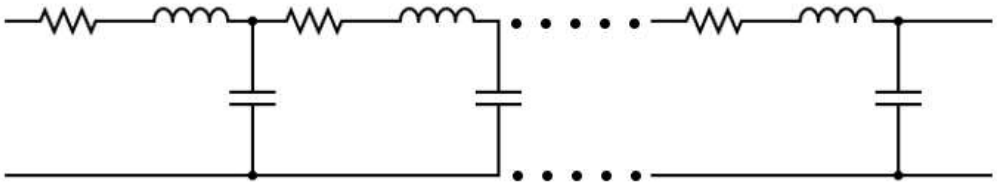


Fig. 5 Transmission Line Circuit Model

In PPU and harness designs, we want to keep the source impedance, which is the combined impedance of the PPU output impedance, the discharge filter impedance, and the harness impedance, as low as possible relative to the HET discharge plasma impedance. Tthe power transfer efficiency to the source and load impedance can be given by

$$\eta = \frac{1}{1 + \frac{Z_S}{Z_L}}. \tag{2}$$

Maximum power transfer occurs when the source and load impedance are equal. Keeping the source impedance lower than the load impedance corresponds to a higher efficiency, while matching source and load impedance gives 50% efficiency.

We show in Figure 6 an inrush current transient from ignition of a 6-kW HET operated at 300 V and 20 A. During this event, the plasma impedance quickly decreases, leading to a fast surge in current [16]. The rising edge of the initial sharp current rise lowers the discharge voltage at the thruster below 300 V, but the discharge voltage never increases beyond 300 V during this event, with the current returning from the ignition peak of 62.5 A to 20 A after ignition. It is important to note that the inrush current can have high-frequency components, which can lead to the harness effectively acting as a transmission line.

The reflection coefficient, which describes how much incident waves are reflected at an end of a transmission line, can be given by

$$\Gamma = \frac{Z_L - Z_0}{Z_L + Z_0}. \tag{3}$$

Wave reflections occur for nonzero reflection coefficients, leading to high discharge voltages exceeding 300 V when waves and reflected waves interfere constructively. It is only during thruster steady state where oscillatory AC current components through the inductor reverse direction, causing the voltage to both drop below and rise above 300 V. However, steady state consists of most dominantly the breathing mode frequency, in the tens of kHz range, which is not high enough for there to be wave reflections from transmission line effects.

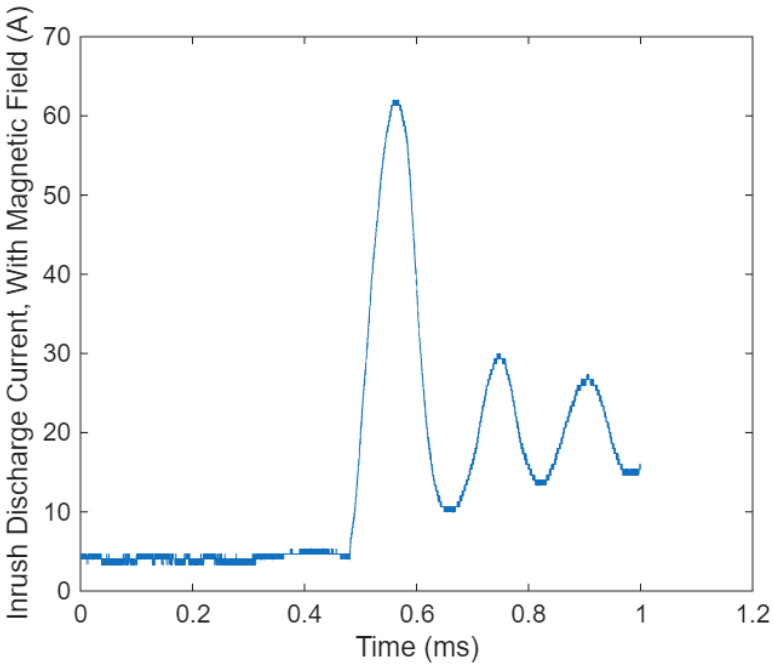


Fig. 6 Inrush Discharge Current with Magnetic Field

This paper presents an experimental and computational effort to characterize the effect of harness inductance on discharge voltage, discharge current, cathode-to-ground, thruster body-to-ground, power supply current, which includes the oscillatory discharge current that is not filtered by the discharge filter, and plasma parameter oscillations. We outline how additional harn ess inductance can act as a form of passive control for the HET system by changing impedance and thus potentially reactive power and power factor, illustrated in Figure 7, rather than simply placing the discharge filter close to the thruster. Inductance control is a more specific case of RLC control, outlined by Barral, which acts as a PID controller. The Kirchhoff's Current Law that relates I_D and the filter parameters R_F, L_F, and C_F [17–20] can be written as

$$I_D = \frac{V_P - V_D}{R_F} + \frac{1}{L_F}\int_0^t (V_P - V_D)\, dt - C_F \frac{dV_D}{dt}. \tag{4}$$

Adjusting L_F can allow for the reduction of I_D. In Equation 4, RF behaves as the proportional gain K_P, LF behaves as the integral gain K_I, and CF behaves as derivative gain K_D. However, the harness inductance does not play the same role as the filter inductance in an RLC filter, as it appears directly in series with the HET load, leading to different impedance effects.

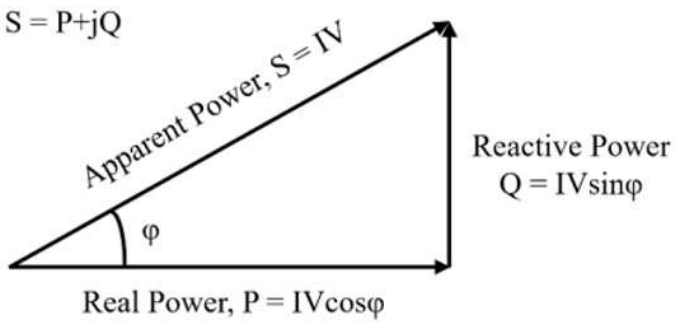


Fig. 7 Power Triangle

V. Methods

In this section we discuss the methods used to conduct harness inductance experiments. Section A discusses the vacuum test facility that was used to conduct experimentation on the HET. Section B discusses the specific thruster used and its setup and operation. Lastly, Section C explains the data collection process.

A. Vacuum Facility

The harness experiment was performed in VTF-2 at Georgia Tech's High-Power Electric Propulsion Laboratory. An image of this facility is shown in Figure 8a. VTF-2 is a stainless-steel chamber measuring 4.9 m in diameter and 9.2 m in length. Rough vacuum in VTF-2 is established using one 495 CFM rotary-vane pump and one 3800 CFM blower. High vacuum is attained using ten liquid nitrogen-cooled CVI TMI re-entrant cryopumps at a pumping speed of 350,000 l/s on xenon. The cryopump shrouds are fed using the Stirling Cryogenics SPC-8 RL special closed-loop nitrogen liquefaction system [21].

B. H6 HET Setup and Operation

We used the H6 HET in this study, shown in Figure 8b, a 6-kW class HET developed in partnership between the NASA Jet Propulsion Laboratory, the Air Force Research Laboratory, and the University of Michigan [1]. The H6 uses a centrally mounted LaB_6 cathode. The thruster body and cathode were isolated from facility ground and were electrically floating.



(a) VTF-2. **(b) H6 HET.**

Fig. 8 VTF-2 and H6 HET

The H6 discharge plasma was controlled using a Magna-Power TS800-24 power supply. The inner and outer electromagnetic coils were powered using TDK-Lambda GEN80-42 power supplies. A TDK-Lambda GEN600-2.6 and GEN60-25 were used to power the cathode keeper and heater, respectively. For protection, the discharge supply was connected to a low-pass RC discharge filter consisting of a series 0.533-Ohm resistor and a shunt 100-μF capacitor to attenuate discharge current oscillations greater than 3 kHz in frequency.

High-purity (99.999%) krypton was fed into the anode and cathode propellant lines using stainless-steel lines metered with MKS GE50A mass flow controllers (MFCs). The MFCs were calibrated by measuring the flow upstream of the thruster with a MesaLabs DryCal 800-10 volumetric flow meter. The uncertainties for flow rates in the anode and cathode lines are 2% and 5%, respectively.

The anode and cathode flow rate and the magnetic field were kept constant during testing. Table 1 shows the H6 HET operating points that were used during experimentation, at discharge voltages of 300 V and 400 V. Upon ignition, the H6 HET was run for three hours until its operating point became steady after outgassing. The base facility pressure was 10 nTorr, while the facility pressure during operation was 2 μTorr. A motorized software-controlled variable inductor was utilized to adjust the inductance in series with the harness at 19 inductance values: 16.6, 19.6, 24.6, 29.6, 34.6, 39.6, 44.6, 49.6, 54.6, 59.6, 64.6, 69.6, 74.6, 79.6, 84.6, 89.6, 94.6, 99.6, 104.6 μH.

Table 1 H6 HET Operating Conditions

Discharge Voltage (V)	Discharge Current (A)	Anode Flow Rate (sccm)	Cathode Flow Rate (sccm)	Inner Coil Current (A)	Outer Coil Current (A)	Breathing Mode Frequency (kHz)
300	4.8	65	6.5	2.94	2.66	8.4
400	4.8	65	6.5	2.94	2.66	12.5

C. Data Collection

The discharge voltage, AC discharge current, cathode-to-ground, thruster body-to-ground, and power supply current oscillations of the H6 HET were recorded using Teledyne LeCroy CP150 and T3CP150 current probes, a Pearson 110A current monitor placed inside VTF2 behind the H6 thruster enclosing the anode line, and HVD3106A and T3HVD1500-70 voltage probes connected to HDO6054 and HDO6104 Teledyne LeCroy oscilloscopes synchronized using an external clock and trigger. The uncertainty and bandwidth of the current probe are ±1% and 10 MHz; for the oscilloscope, they are ±0.5% full scale and 1 GHz. The oscilloscope has 12 bits of resolution with a selected 25 MS/s sampling rate and is used over an interval of 10 ms for a total of 250,000 samples. MATLAB instrument control toolbox with USB and Ethernet for remote desktop were used for semi-automated data collection. Thruster data was taken after it was observed that the PP discharge current values had stopped changing within ±1% variation, taking approximately two hours.

Systematic and random errors were quantified as part of this study's error analysis. Systematic errors are introduced by voltage and current probe measurement uncertainty, along with the oscilloscope's uncertainty in the acquired data. These uncertainties were defined in the data collection subsection.

VI. Results and Discussion

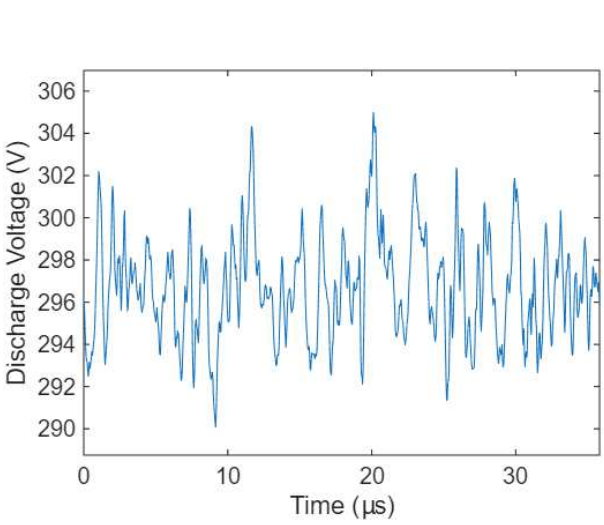
We first present time-domain and frequency-domain plots of discharge voltage, discharge current, cathode-to-ground voltage, and thruster body-to-ground voltage at both the 300 V and 400 V operating points at the minimum inductance of 16.6 μH to provide context on what the waveforms of interest look like before showing the effects of varying the harness inductance.

We then present results on the electrical effects of varying harness inductance on the HET discharge plasma. For both the 300 V and 400 V conditions, we show RMS plots of discharge voltage, discharge current, cathode-to-ground voltage, thruster body-to-ground voltage, mean plots of cathode-to-ground voltage and thruster body-to-ground voltage, and a PP plot of power supply current, all as a function of harness inductance. To better aid analysis, we plot mean normalized quantities for better comparison between the two operating points. The breathing mode frequency is determined from the FFT of the discharge current as the dominant peak.

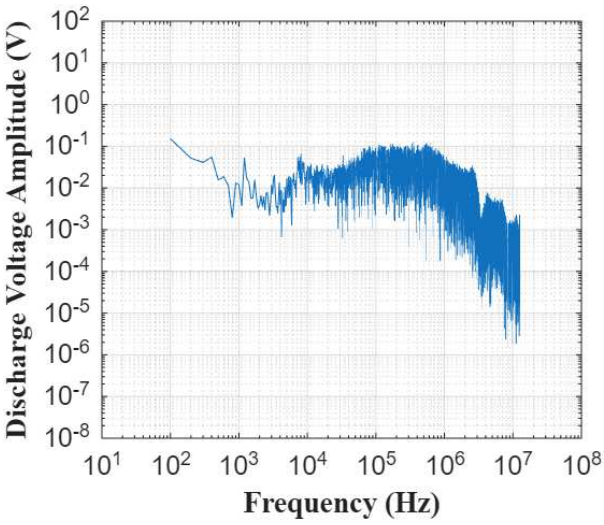
Lastly, we use the extended Kalman filter to estimate plasma parameters from electrical measurements, which constitute our aim to understand circuit-plasma coupling for HETs. We examine these plasma parameters in the time domain while also understanding their dependence on the harness inductance. We show that both electrical and plasma parameters have a nonlinear dependence on harness inductance.

A. Discharge Voltage and Discharge Current at a Fixed Harness Inductance

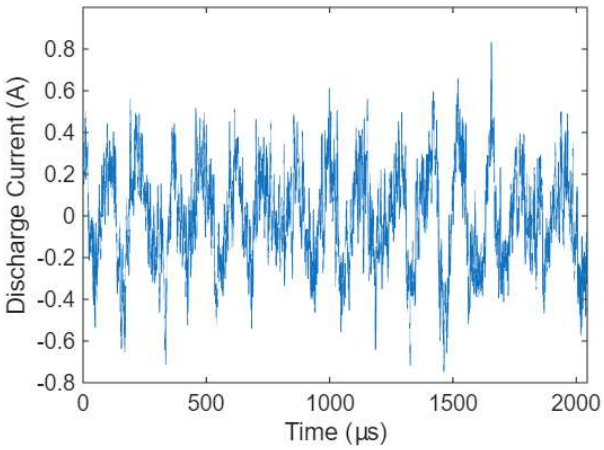
Figure 9 shows the discharge voltage and discharge current in the time and frequency domains at the 300 V operating point with 16.6 μH of harness inductance. At this operating point, we can see that the discharge voltage and discharge current are not significantly oscillatory compared to the other operating modes, having a peak-to-peak discharge voltage of 15 V (5% of the mean) and a peak-to-peak AC discharge current of 1.6 A (33% of the mean), as shown in Figs. 9a(a) and (c), respectively. The breathing mode frequency is close to 7.5 kHz, which can be seen from Fig. 9c(d), with a weak breathing mode peak in the discharge current FFT. The discharge voltage FFT in Fig. 9b(b) shows a small peak at the breathing mode frequency, however, lower frequencies less than 1.5 kHz and higher frequency components greater than 500 kHz have amplitudes that exceed the breathing mode amplitude.



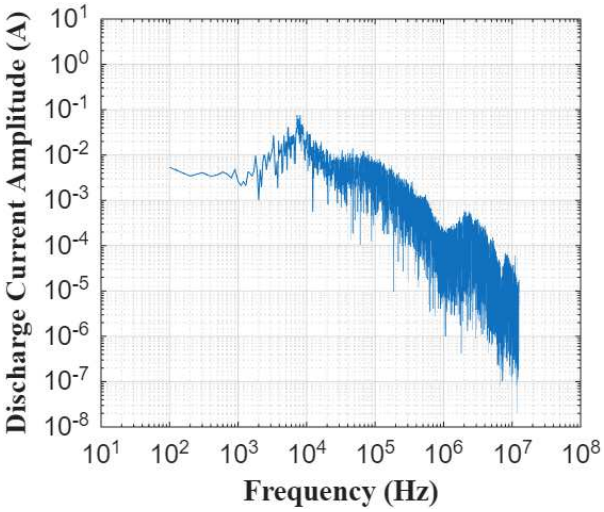
(a) Discharge Voltage as a Function of Time



(b) Discharge Voltage FFT



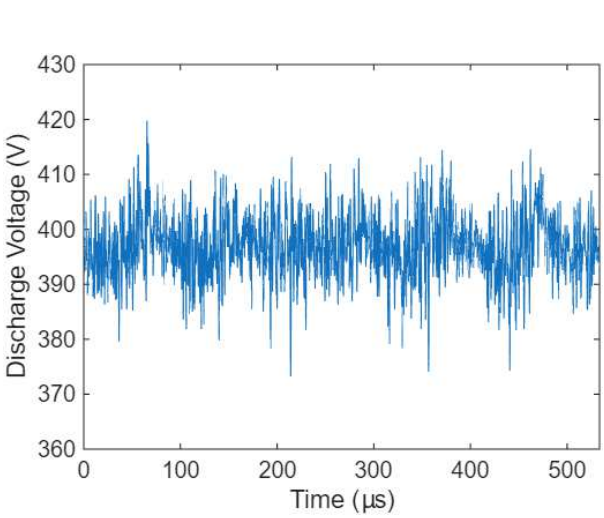
(c) Discharge Current as a Function of Time



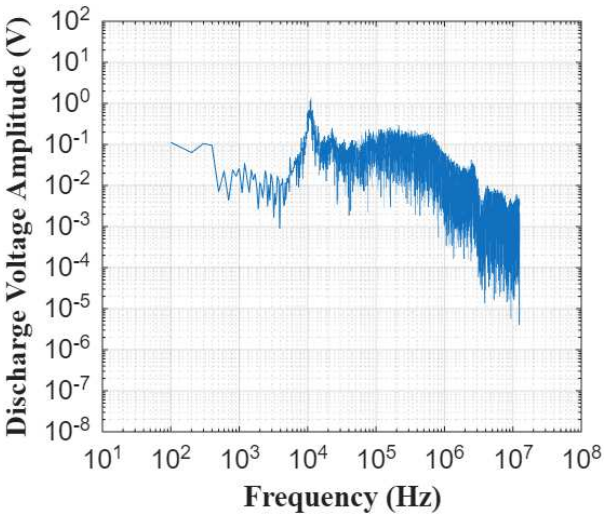
(d) Discharge Current FFT

Fig. 9 Discharge Voltage and Discharge Current at 300 V Operating Point With 16.6 µH Harness Inductance

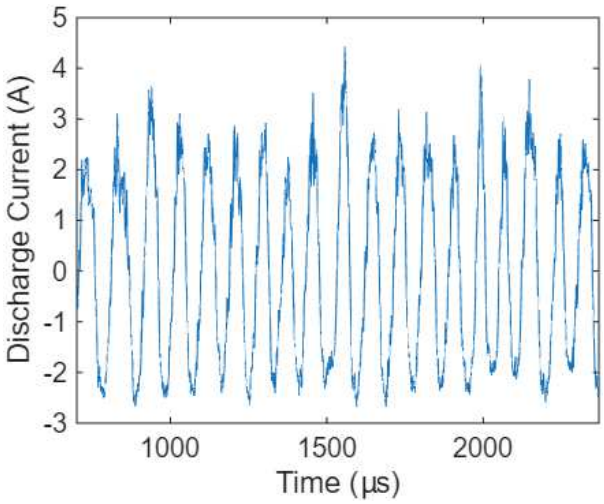
Figure 10a and Figure 10c show the discharge voltage and discharge current in the time domain at the 400 V operating point with 16.6 μH of harness inductance. At this operating point, we can see that the discharge voltage and discharge current are more oscillatory, having a peak-to-peak discharge voltage of 40 V (10% of the mean) and a peak-to-peak AC discharge current of 7 A (146% of the mean). The breathing mode frequency is close to 11 kHz, which can be seen in Figure 10b and Figure 10d, and is more pronounced as opposed to the 300 V case in both the discharge voltage and discharge current FFTs.



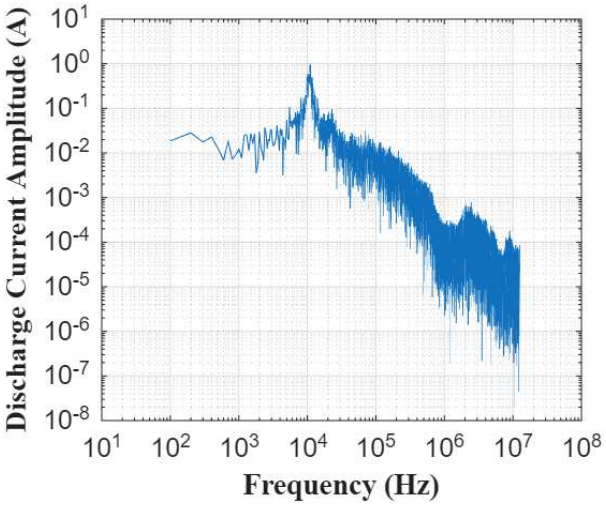
(a) Discharge Voltage as a Function of Time



(b) Discharge Voltage FFT



(c) Discharge Current as a Function of Time

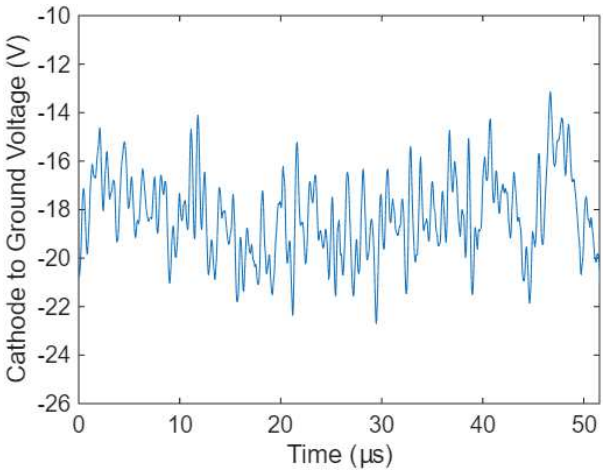


(d) Discharge Current FFT

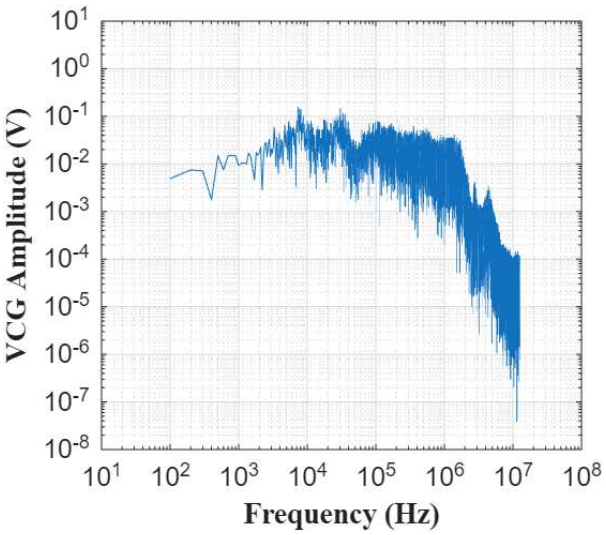
Fig. 10 Discharge Voltage and Discharge Current at 400 V Operating Point With 16.6 µH Harness Inductance

B. Cathode-to-Ground Voltage and Thruster Body-to-Ground Voltage at a Fixed Harness Inductance

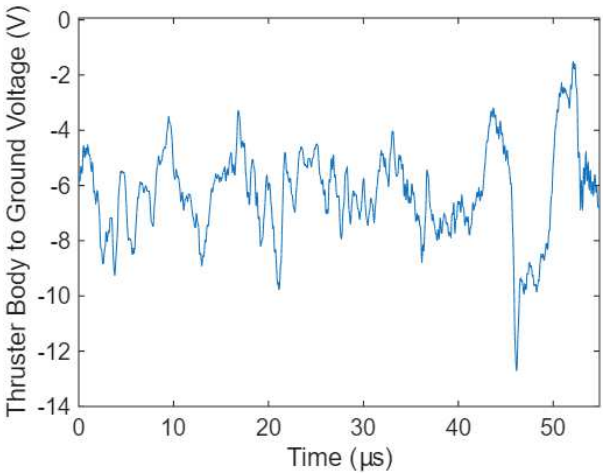
Figure 11a and Figure 11c show the cathode-to-ground voltage (VCG) and the thruster body-to-ground voltage (VTBG) in the time domain at the 300 V operating point with 16.6 μH of harness inductance. At this operating point, we can see that VCG has a peak-to-peak of 8 V, while VTBG has a peak-to-peak of approximately 14 V. The mean VCG is -17.75 V, while the mean VTBG is -6 V. As shown in Figure 11b and Figure 11d, their FFTs do not appear to have a single dominant peak. This may indicate that VCG and VTBG are uncorrelated to the discharge voltage and current [22].



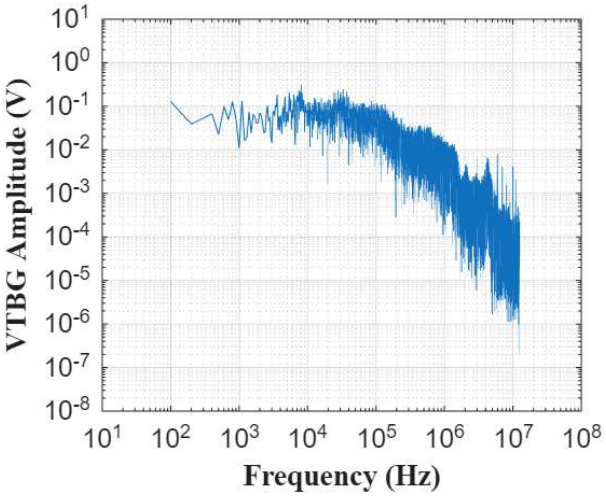
(a) Cathode-to-Ground Voltage as a Function of Time



(b) Cathode-to-Ground Voltage FFT



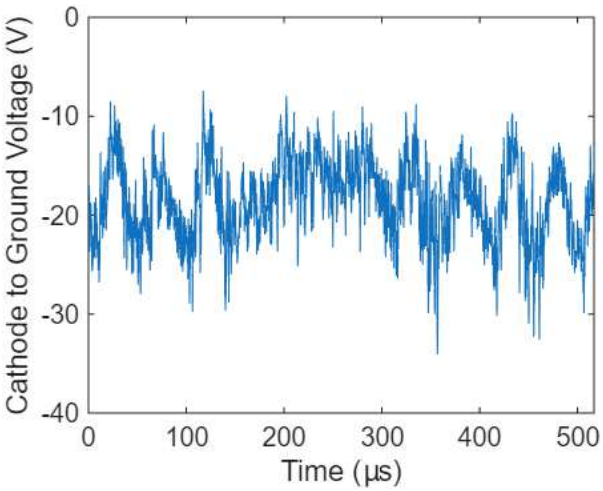
(c) Thruster Body-to-Ground Voltage as a Function of Time



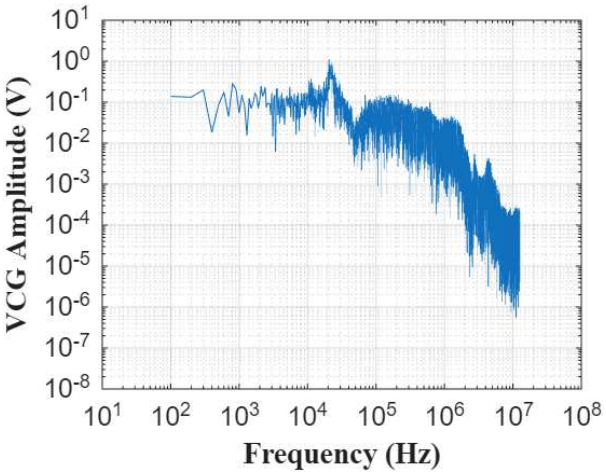
(d) Thruster Body-to-Ground Voltage FFT

Fig. 11 Cathode-to-Ground Voltage and Thruster Body-to-Ground Voltage at 300 V Operating Point With 16.6 µH Harness Inductance

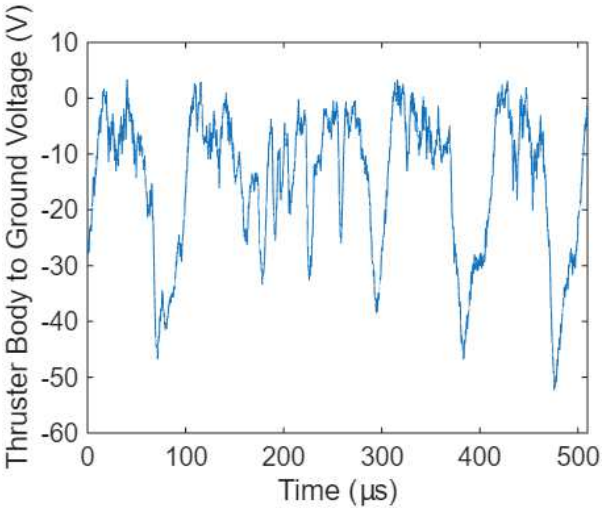
Figure 12a and Figure 12c shows VCG and the VTBG in the time domain at the 400 V operating point with 16.6 μH of harness inductance. At this operating point, we can see that VCG has a peak-to-peak of 20 V, while VTBG has a peak-to-peak of approximately 50 V. The mean VCG is -18.65 V, while the mean VTBG is -16 V. As shown in Figure 12b and Figure 12d, their FFTs now have single dominant peaks as opposed to the 300 V operating condition, suggesting that the discharge plasma oscillation is coupled to the thruster body. It is interesting to note that VCG's FFT shows a dominant peak close to 20 kHz, different than the breathing mode frequency of 11 kHz, indicating that cathode plasma dynamics may differ from that of the main discharge.



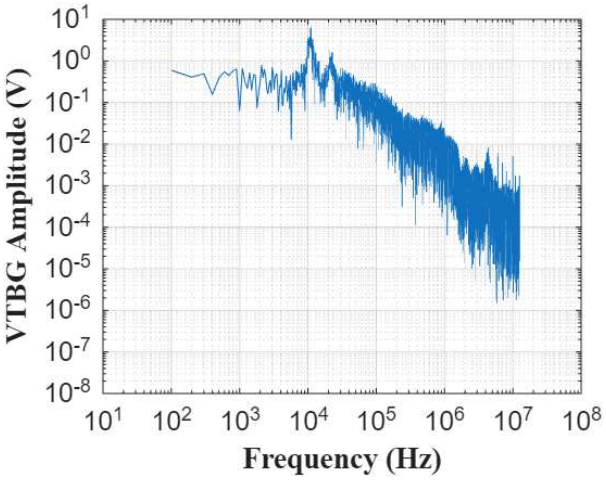
(a) Cathode-to-Ground Voltage as a Function of Time



(b) Cathode-to-Ground Voltage FFT



(c) Thruster Body-to-Ground Voltage as a Function of Time

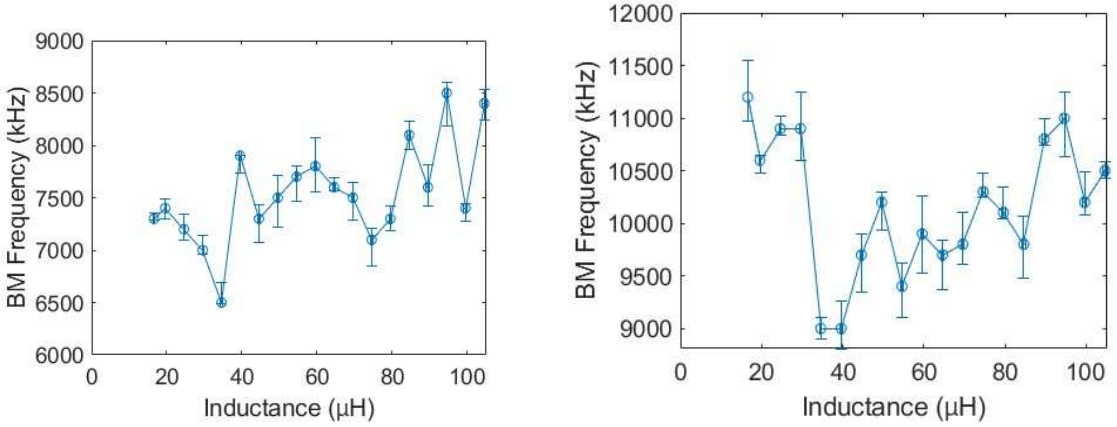


(d) Thruster Body-to-Ground Voltage FFT

Fig. 12 Cathode-to-Ground Voltage and Thruster Body-to-Ground Voltage at 400 V Operating Point With 16.6 µH Harness Inductance

C. Effects of Harness Inductance

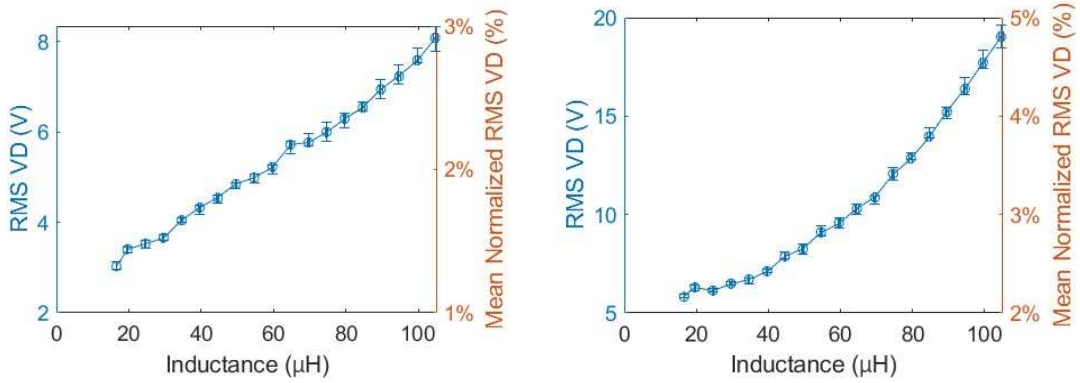
Figure 13a shows that the BM frequency attains a minimum of 6.5 kHz at 34.6 μH and a maximum of 8.5 kHz at 89.6 μH at 300 V, corresponding to a roughly linear characteristic between BM frequency and inductance. A possible explanation for this result is the weaker BM peak seen in the FFT at this operating point, which does not correspond to strong and nonlinear BMs with large peaks. At 400 V, Figure 13b shows that a minimum of 9 kHz is attained at 34.6 μH and 39.6 μH, with a maximum of 11.25 kHz at 16.6 μH. In contrast to the 300 V case, the 400 V case shows a reduction in BM frequency from 16.6 μH to 34.6 μH, followed by a roughly linear increase until 104.6 μH at 10.5 kHz.



(a) 300 V Case **(b) 400 V Case**

Fig. 13 BM Frequency as a Function of Inductance

Figure 14a and Figure 14b show that the RMS of the discharge voltage oscillations increase with increasing inductance, as expected from the equation $V = L\frac{dI}{dt}$. The 300 V RMS ranges from 3 V to 8 V across the inductance range, whereas the 400 V RMS ranges from 6 V to 19 V. However the 400 V curve appears to be nonlinear while the 300 V curve appears to be linear. It is important to note that the RMS normalized by the oscillation mean does not match between operating conditions, where at 300 V percentages range from 2% to 3%, whereas for 400 V percentages range from 2% to 5%. The 400 V operating condition is more oscillatory with a higher BM frequency, which results in a larger percentage of the mean oscillation.



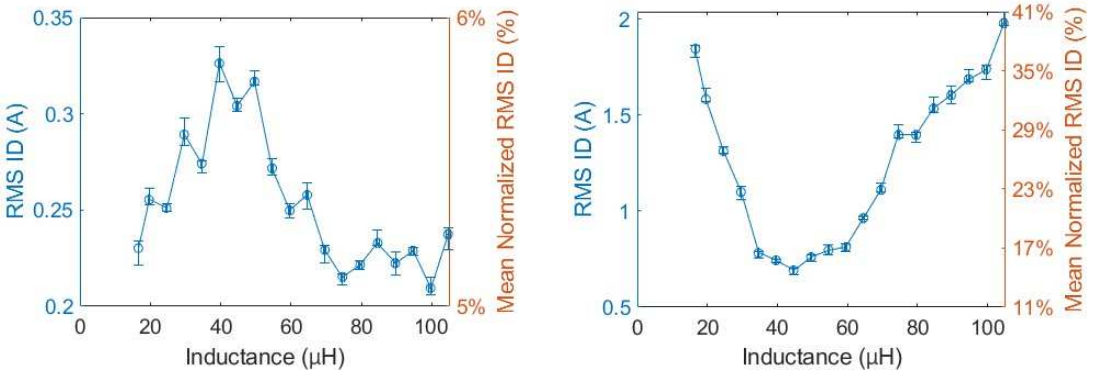
(a) 300 V Case **(b) 400 V Case**

Fig. 14 RMS Discharge Voltage as a Function of Inductance

Figure 15a shows that the RMS discharge current at 300 V increases to a maximum of 0.325 A at around 39.6 μH of inductance, then continues to decrease as inductance increases. On the other hand, the 400 V condition shown in Figure 15b reaches a minimum RMS of 0.7 A, respectively, at 44.6 μH, rather than a maximum, then begins increasing with increasing inductance. The 300 V RMS ranges from 0.21 A to 0.33 A across the inductance range, whereas the 400 V RMS ranges from 0.7 A to 2 A. Again, the RMS normalized by the oscillation mean does not match between operating conditions, where at 300 V percentages range from 5% to 5.8% for RMS, whereas for 400 V the RMS ranges from 16% to 41%. It is clear that the 400 V operating condition is more oscillatory, which results in a larger percentage of the mean oscillation.

The current oscillations are maximized for the 300 V case and minimized for the 400 V case at 39.6 μH and 44.6 μH, respectively, due to nonlinear impedance interactions with the HET impedance. The breathing mode frequency is minimized at 9 kHz in the 400 V case. Harness inductance can be seen as exchanging magnetic energy with the

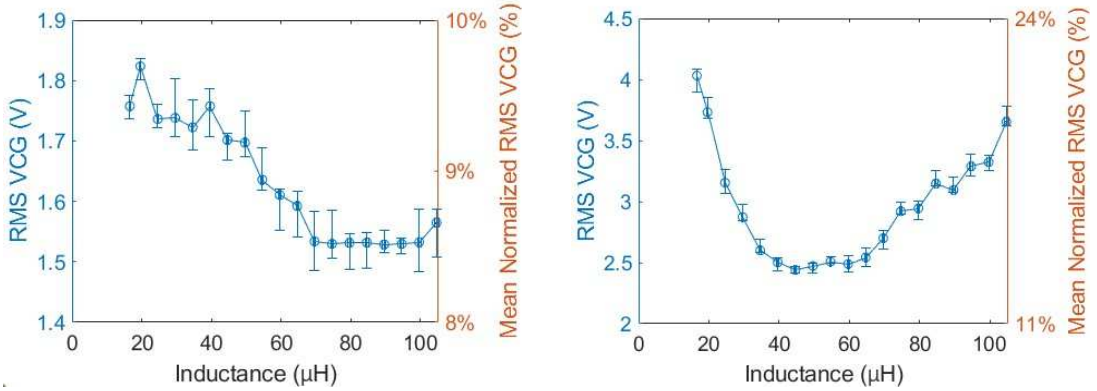
discharge plasma. In the linear case, the harness inductance sets the phase shift between the discharge voltage and the discharge current, which furthermore sets the timing of breathing mode physics. With the appropriate phase shift, it can be seen that the harness inductance creates a voltage wave that either constructively or destructively interferes to various extents with the existing discharge voltage oscillation, resulting in increases or decreases in discharge current oscillation amplitude. As the plasma becomes more nonlinear, the concept of constructive and destructive interference with linear waves no longer holds, and we instead must consider other basis functions such as intrinsic mode functions that represent nonlinear and instantaneous amplitude, frequency, and phase that can be more difficult to intuitively explain [15]. Plasma state estimation could provide more information about the plasma dynamics associated with the electrical dynamics that result from changing the harness inductance.



(a) 300 V Case **(b) 400 V Case**

Fig. 15 RMS Discharge Current as a Function of Inductance

Figure 16a shows that the RMS cathode-to-ground voltage at 300 V attains a minimum of 1.525 V between 64.6 and 99.6 µH. On the other hand, the 400 V condition shown in Figure 16b reaches a minimum RMS of 2.5 V at 44.6 μH, which is tied to improved electron emission. The 300 V RMS ranges from 1.525 V to 1.825 V across the inductance range, whereas the 400 V RMS ranges from 2.41 V to 4.1 V. At 300 V, mean normalized RMS percentages range from 9.1% to 9.7%, whereas for 400 V RMS percentages ranges from 15% to 19.5%. It is not quite clear why 89.6 μH minimizes the oscillations at 300 V.

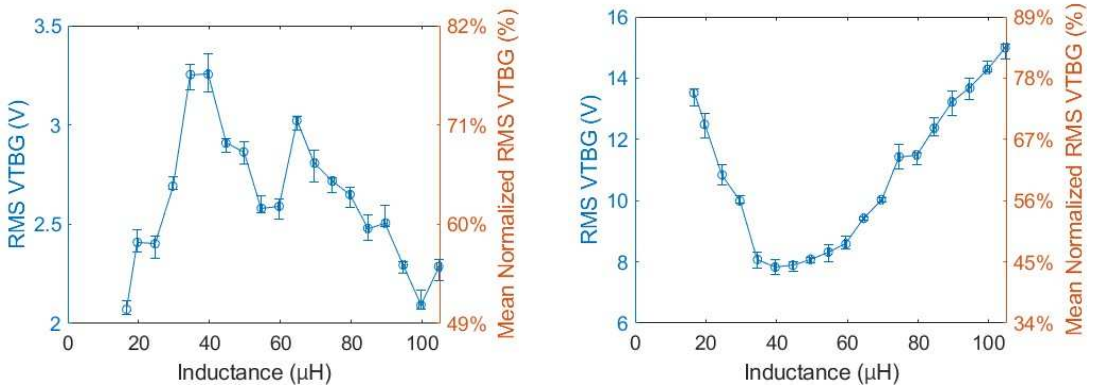


(a) 300 V Case **(b) 400 V Case**

Fig. 16 RMS Cathode-to-Ground Voltage as a Function of Inductance

Figure 17a shows that at 300 V, the RMS thruster body-to-ground voltage increases to a peak of 3.3 V at 39.6 μH, then decreases. On the other hand, the 400 V condition shown in Figure 17b reaches a minimum RMS of 8 V at 39.6 μH. The 300 V RMS ranges from 2.07 V to 3.3 V across the inductance range, whereas the 400 V RMS ranges from 8

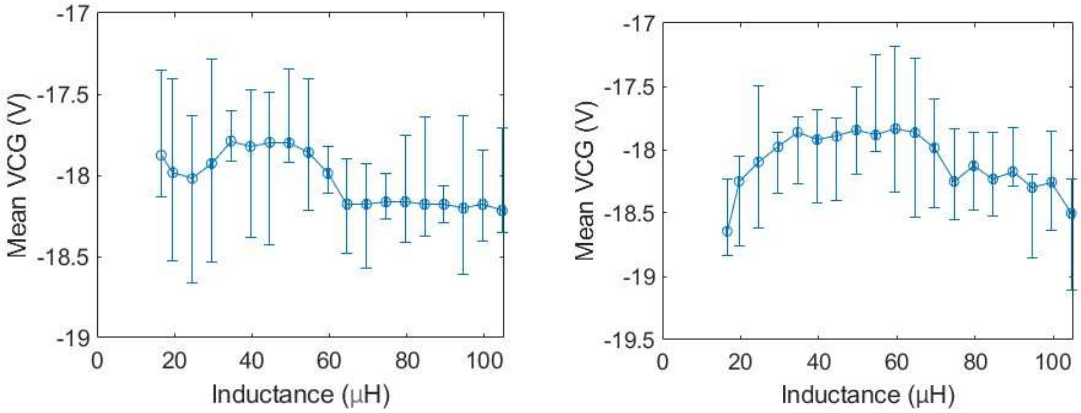
V to 15 V. For the RMS at 300 V, the mean normalized percentages range from 54% to 76% for RMS, whereas for 400 V the RMS ranges from 44% to 85%.



(a) 300 V Case **(b) 400 V Case**

Fig. 17 RMS Thruster Body-to-Ground Voltage as a Function of Inductance

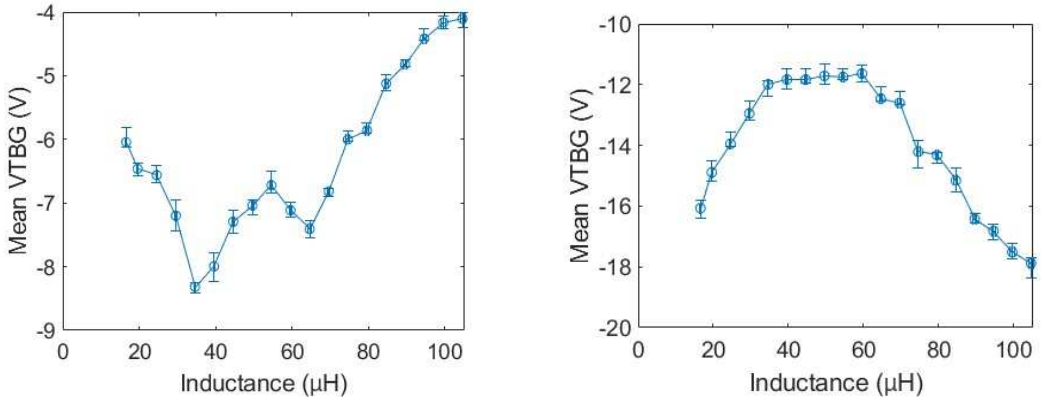
Figure 18a shows that at 300 V the mean cathode-to-ground voltage reaches a maximum of -17.78 V at 29.6 μH, then decreases to -18.2 V at 64.6 μH, where it then stays relatively constant until 104.6 μH. At 400 V, shown in Figure 18b, the mean cathode-to-ground voltage reaches a maximum of -17.825 V at around 44.6 μH from a minimum of -18.625 V at 19.6 μH, and then begins to decrease. It is evident that the 400 V operating condition has roughly the same mean cathode-to-ground voltage of -18 V as the 300 V condition.



(a) 300 V Case **(b) 400 V Case**

Fig. 18 Mean Cathode-to-Ground Voltage as a Function of Inductance

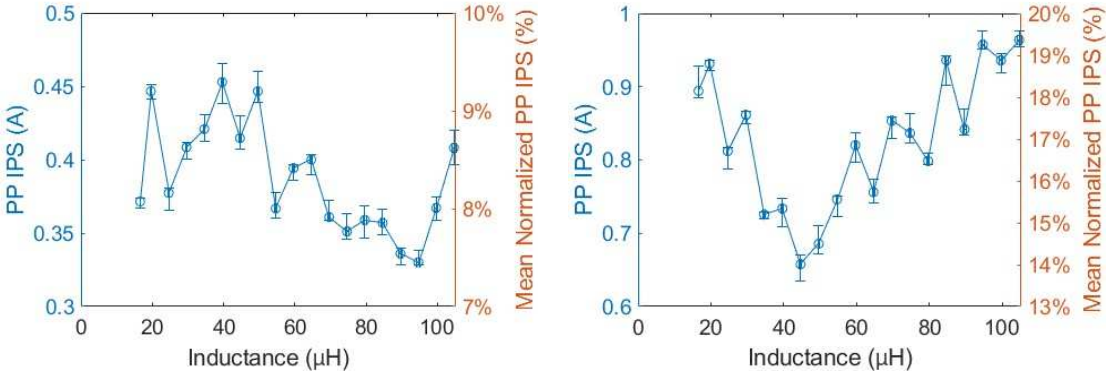
Figure 19a shows that the mean thruster body-to-ground voltage reaches a minimum of -8.5 V at around 34.6 μH and increases to a maximum of -4.1 V at 104.6 μH. At 400 V, shown in Figure 19b, the mean thruster body-to-ground voltage has a maximum of around -11.75 V at 44.6 μH, then continues to decrease to a minimum of -18 V at 104.6 μH at 400 V. The thruster mean body-to-ground voltage is lower at 400 V at around -14 V on average as opposed to -6.5 V on average at 300 V. This suggests that the thruster body is at a much lower potential than ground at 400 V, which would indicate there to be more ion current flow from the plasma to the thruster body.



(a) 300 V Case **(b) 400 V Case**

Fig. 19 Mean Thruster Body-to-Ground Voltage as a Function of Inductance

Figure 20a shows that the PP power supply current at 300 V reaches a minimum of 0.33 A at 94.6 μH compared to a maximum of 0.45 A at 39.6 μH. Figure 20b shows that at 400 V the PP power supply current reaches a minimum of 0.65 A at 44.6 μH compared to a maximum of 0.97 A at 104.6 μH. For the PP at 300 V, the mean normalized percentages range from 7.4% to 9%, whereas for 400 V the PP ranges from 15% to 19.5%. These results show that the power supply current oscillations do in fact change with harness inductance. It is possible to use harness inductance as an additional filter that could further protect the PPU.



(a) 300 V Case **(b) 400 V Case**

Fig. 20 PP Power Supply Current as a Function of Inductance

VII. Circuit-plasma coupling

In this section, we discuss the coupling between the discharge circuit and the discharge plasma. We hypothesize that the nonlinear behavior of the discharge current and voltage oscillations as the harness inductance is changed is due to the coupling between the discharge circuit and the HET plasma. To better understand the underlying plasma physics, a zero-dimensional (0D) global plasma model of a HET is used in conjunction with an extended Kalman filter (EKF) to provide estimates of spatially-averaged, time-resolved plasma properties [12, 23, 24].

A. Global plasma model

The 0D global model consists of the ion and neutral continuity equations and the electron energy equation:

$$\frac{\partial N_i}{\partial t} + \frac{N_i U_i}{L_p} + \frac{2N_i U_{i,w}}{R_\Delta} = N_i N_n \zeta_{ion}, \tag{5}$$

$$\frac{\partial N_n}{\partial t} + \frac{(N_n - N_{int})U_n}{L_p} = -N_i N_n \zeta_{ion}, \tag{6}$$

$$\frac{\partial}{\partial t}\left(\frac{3}{2}N_i T_e\right) + \frac{5}{2}\frac{N_i U_e T_e}{L_p} = S_j - S_w - S_c, \tag{7}$$

where the ion bulk velocity is approximated as $U_i = \sqrt{eV_d/M_i}$, e is the elementary charge, V_d is discharge voltage, M_i is ion mass, and $U_{i,w}$ is the ion bulk velocity towards the wall accounting for radial ion losses [11]. Here, $U_{i,w} = \sqrt{eT_e/M_i}$ is the Bohm velocity, T_e is the electron temperature in eV, R_Δ is the channel width, $N_{int} = \dot{m}(M_i A_c U_n)^{-1}$ is the number density of neutral particles injected at the anode, U_n is the neutral bulk velocity which is assumed to be constant, A_c is the thruster cross-sectional area, $\dot{m}$ is the mass flow rate, and ζ_{ion} is the ionization rate, given as

$$\zeta_{ion} = \sqrt{\frac{8eT_e}{\pi m_e}}\left[A_i T_e^2 + B_i \exp\left(-\frac{C_i}{T_e}\right)\right], \tag{8}$$

where for krypton, $A = -1.1592 \times 10^{-24}$, $B = 4.9527 \times 10^{-20}$, $C = 14.0$, and m_e is the mass of an electron. The coefficients A, B, and C for krypton are determined by fitting to rate coefficient data obtained from the Biagi database [25], assuming a Maxwellian electron energy distribution function. The ionization rate coefficient and fitting function are shown in Fig. 21. The proposed fitting function follows the procedure used for xenon in Ref 2. In equation (7), $S_j = -N_i U_e E$ is the energy gain due to Joule heating, U_e is the electron bulk velocity, $E \approx V_d/L_p$ is the electric field strength, $S_w = N_i \epsilon_w \nu_w$ is the energy loss due to interactions with the channel wall, $S_c = \chi N_i N_n \zeta_{ion} \epsilon_{ion}$ is the energy loss due to inelastic ion collisions, χ is the ionization cost accounting for inelastic energy loss, and ϵ_{ion} is the energy loss of electrons due to ionization. The ionization cost is assumed to be a constant value. The wall collision frequency is given as

$$\nu_w = \frac{1}{R_\Delta}\sqrt{\frac{eT_e}{M_i}}\frac{1}{1-\sigma}, \tag{9}$$

where σ is the effective rate of secondary electron emission. For krypton and boron nitride channel walls, at $T_e \leq 24.5\ eV$, $\sigma = T_e/25$, otherwise the sheath is considered to be space charge limited (SCL) and $\sigma = 0.979$ [26]. The energy loss to the wall is described as

$$\epsilon_w = 2T_e + (1-\sigma)\phi_w, \tag{10}$$

where

$$\phi_w = T_e \ln \frac{1-\sigma}{\sqrt{2\pi m_e/M_i}} \tag{11}$$

is the sheath potential [9, 10, 27].

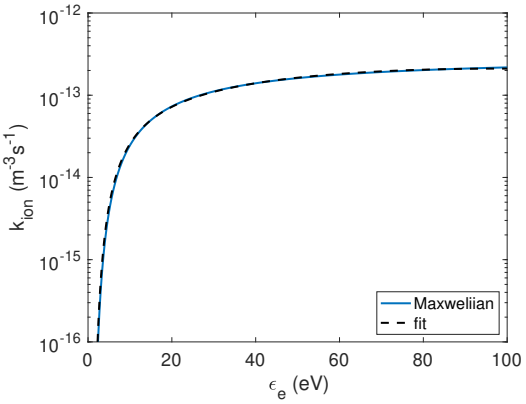


Fig. 21 Ionization rate coefficient and approximate fitting function for krypton.

The discharge current in the channel of the HET, which will be used as the measurement signal for the EKF, can be calculated as

$$I_d = eA_c N_i \left(U_i - U_e\right). \tag{12}$$

After data assimilation, the cross-field electron mobility can be estimated as $\mu_\perp \approx -U_e/E$ assuming that the drift due to the electric field dominates over that of the pressure gradient, which cannot be captured in a 0D model.

B. Extended Kalman Filter

State estimation combines measurements and system model predictions to better determine the values of the next set of states. This allows for models that may not perfectly capture the dynamics. We employ a Kalman filter for state estimation based on discharge current measurements to improve the state estimates for our discharge plasma system, using prediction and correction.

For a dynamical system with a state vector $\boldsymbol{x}(t)$, the extended Kalman filter (EKF) consists of an estimated state vector $\hat{\boldsymbol{x}}(t)$, measurement vector $\tilde{\boldsymbol{y}}(t)$, system covariance matrix $P(t)$, measurement noise covariance matrix $R(t)$, process noise covariance matrix $Q(t)$, and noise gain matrix $G(t)$, where each of these quantities can depend on time. The goal of the EKF is to provide an estimate of the underlying states as functions of time which reproduce $\tilde{\boldsymbol{y}}(t)$. At some discrete timestep, k, when the model acquires a measurement, *i.e.*, data, the predicted state denoted with (-) will be corrected to an updated state denoted using (+), as follows:

$$\hat{\boldsymbol{x}}_k^+ = \hat{\boldsymbol{x}}_k^- + K_k \left[\tilde{\boldsymbol{y}}_k - \boldsymbol{h}\left(\hat{\boldsymbol{x}}_k^-\right)\right], \tag{13}$$

$$P_k^+ = [\mathbb{I} - K_k H_k(\hat{\boldsymbol{x}}_k^-)]P_k^-, \tag{14}$$

where $\mathbb{I}$ is the identity matrix, $\boldsymbol{h}$ is the vector of measurement equations, $H_k\left(\hat{\boldsymbol{x}}_k^-\right) = \partial \boldsymbol{h}/\partial \boldsymbol{x}|_{\hat{\boldsymbol{x}}_k^-}$ is the measurement Jacobian matrix, and K_k is the Kalman gain, calculated as

$$K_k = P_k^- H_k^T\left(\hat{\boldsymbol{x}}_k^-\right)\left[H_k\left(\hat{\boldsymbol{x}}_k^-\right) P_k^- H_k^T\left(\hat{\boldsymbol{x}}_k^-\right) + R_k\right]^{-1}. \tag{15}$$

Here, the continuous-discrete EKF is used. Rather than apply equations (13) and (14) at each timestep, a set of equations, i.e., Eqs. (5)-(7), are used to govern the continuous propagation of states between the arrival of measurement data at some discrete time. This set of equations can be interpreted as a physical model of the expected system dynamics and is generally given as

$$\dot{\hat{\boldsymbol{x}}} = \boldsymbol{f}(\hat{\boldsymbol{x}}, t), \tag{16}$$

$$\dot{P} = F(\hat{\boldsymbol{x}}, t)P + PF^T(\hat{\boldsymbol{x}}, t) + GQG^T, \tag{17}$$

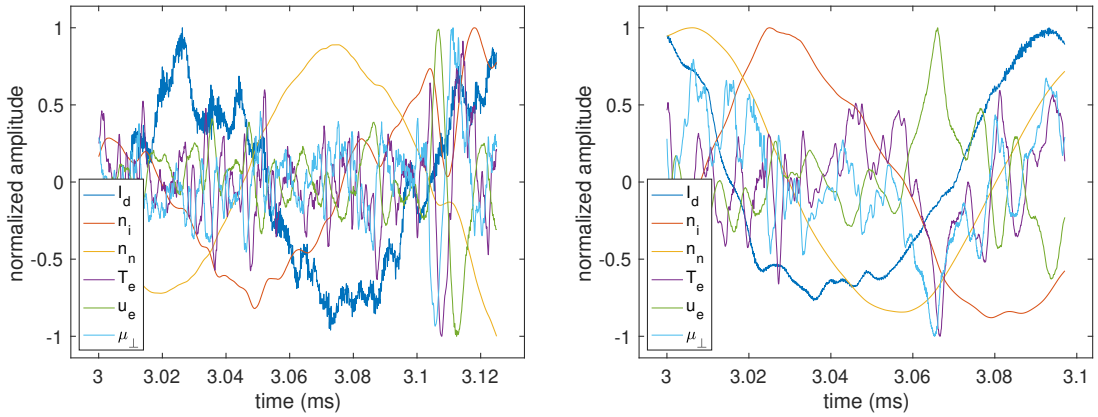
where $\boldsymbol{f}$ is the dynamics model function of the state variables and $F(\hat{\boldsymbol{x}}, t) = \partial \boldsymbol{f}/\partial \boldsymbol{x}|_{\hat{\boldsymbol{x}}}$ is the Jacobian matrix of the dynamics model. The combination of Eqs. (13)-(14) and (16)-(17) can be viewed as a predictor-corrector method, where Eqs. (16)-(17) describe the continuous propagation in time of the state quantities through the dynamics (physics-based) model and equation (13)-(14) augment the state values based on the measurement.

For this analysis, the state variables for the EKF are taken to be $\boldsymbol{x} = [N_i\ N_n\ T_e\ U_e]^T$. The electron velocity, U_e, is considered to be an unknown parameter and therefore is only updated when a new measurement arrives (i.e., $dU_e/dt = 0$). A provided discharge current signal is used as the measurement signal, $\tilde{\boldsymbol{y}} = \tilde{I}_d$, and is estimated using equation (12). Here, $\boldsymbol{f}$ is defined by Eqs. (5), (6), and (7) as well as $\partial U_e/\partial t = 0$, and $\boldsymbol{h}(\boldsymbol{x})$ is given by equation (12).

C. State estimation results

The fusion of the experimental data (i.e., discharge current and discharge voltage) with the 0D global plasma model using the EKF allows for the estimation of spatially-averaged, time-resolved plasma properties. The model is run for each combination of harness inductance and operating condition, yielding 38 separate simulations. Examples of the time-resolved state estimates are shown in Figs. 22a and 22b for a harness inductance of 100 μH for the 300 V and 400 V cases, respectively. Each plot shows the normalized waveform of the experimental discharge current trace alongside those of the estimated ion number density, neutral number density, electron temperature, electron bulk velocity, and electron cross-field mobility. Although the details of the oscillations vary with harness inductance and operating condition, several qualitative observations remain constant. The waveforms show predominantly low-frequency (BM) sinusoidal behavior in the discharge current, ion number density, and neutral number density, and high-frequency

non-sinusoidal behavior in the electron temperature, electron bulk velocity, and cross-field electron mobility. This implies that the BM oscillation is largely driven by the predator-prey interaction between ions and neutrals, consistent with previous findings [9]. Appendix shows the unnormalized plasma state and parameter estimation.



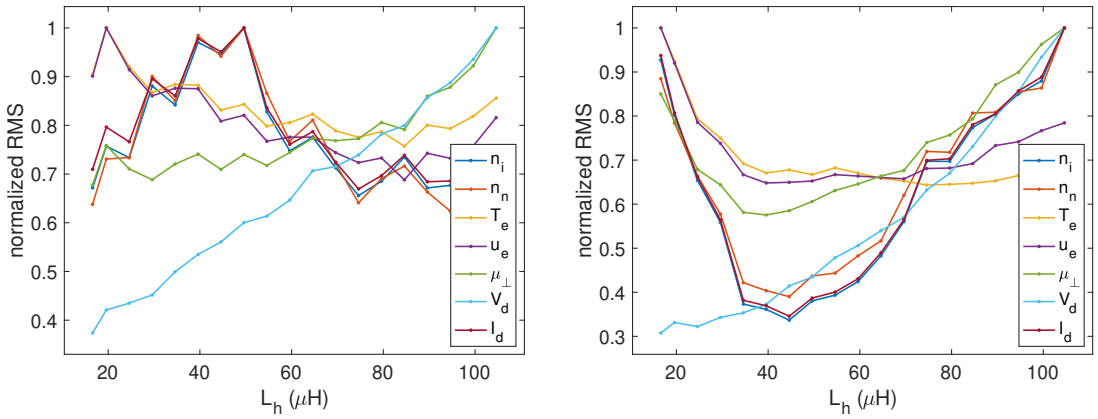
(a) Waveforms with 100 μH harness at 300 V **(b) Waveforms with 100 μH harness at 400 V**

Fig. 22 Plots of the normalized waveforms for the experimental discharge current and estimated ion number density, neutral number density, electron temperature, electron bulk velocity, and electron cross-field mobility as functions of time with 100 μH harness inductance at (left) 300 V and (right) 400 V.

A more convenient way to visualize the dependence of the plasma oscillations on the harness inductance is by comparing the normalized RMS oscillation amplitudes of all quantities, as is shown in Figs. 23a and 23b for the 300 V and 400 V case, respectively. The discharge currents and discharge voltages shown in these figures correspond to those in Figs. 14 and 15. At both operating conditions, Figs. 23a and 23b show that the ion and neutral number densities normalized RMS amplitudes closely follow the trend of the discharge current, consistent with the waveforms shown in Figs. 22a and 22b. At 300 V, Fig. 23a demonstrates that the electron temperature normalized RMS amplitudes tend to decrease with increased harness inductance but reach a minimum at around 85 μH. The cross-field mobility increases slowly, mostly staying at a normalized RMS of 0.7 at low inductance, then closely follows the trend of the discharge voltage beginning at around 85 μH. This change in the oscillatory behavior of the electron properties may suggest an increased coupling between the plasma and circuit at large harness inductance.

As shown in Fig. 22b, the behavior at 400 V appears to be more nonlinear, showing approximately the same RMS oscillation amplitude for the discharge current, ion density, and neutral density at 15 μH and 105 μH with a large decrease in between. The discharge voltage RMS oscillation amplitude again increases with harness inductance, but no longer linearly. The electron temperature and electron velocity RMS oscillation amplitudes sharply decrease from a normalized RMS of 1 at 16.6 μH to 0.7 at 40 μH before plateauing. The electron velocity RMS oscillation amplitude then increases slightly with harness inductance. Perhaps most interesting is the cross-field electron mobility, which qualitatively follows the discharge current in shape but does not experience as large a decrease in RMS oscillation amplitude.

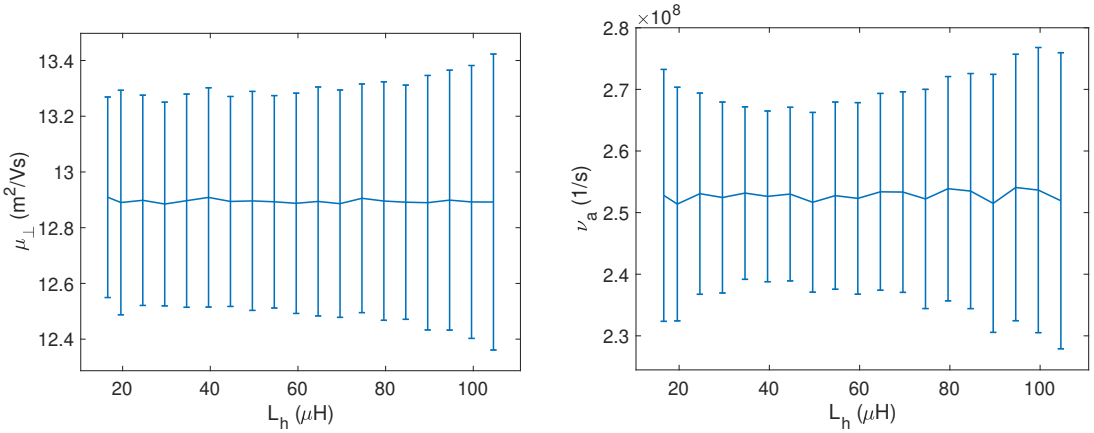
The ion number density and electron velocity are minimized at 40 μH while the ion velocity increases with discharge voltage with increasing harness inductance. This leads to a minimum in discharge current oscillations, which can be observed in earlier plots. In the linear case, phase alignment between ion number density, ion velocity, and electron velocity lead to greater discharge current oscillations, whereas phase misalignment leads to lower discharge current oscillations. In the nonlinear case, the concept of phase becomes more murky and it is hard to associate changes in timing between plasma parameters to changes in discharge current oscillations.



(a) State RMS amplitudes at 300 V **(b) State RMS amplitudes at 400 V**

Fig. 23 Normalized RMS oscillation amplitudes for all estimated plasma properties, along with the discharge current and discharge voltage, at (left) 300 V and (right) 400 V operating conditions.

Figures 24a and 24b show the dimensional cross-field mobility as a function of harness inductance, with the error bars indicating the amplitude of the RMS oscillations. Here, it can clearly be seen that the time-averaged cross-field mobility is constant with harness inductance. This implies that the harness length does not affect the resistance of the plasma, but only its reactance. This interaction further implies nonlinear coupling between the linear circuit upstream of the thruster and the plasma load.



(a) Electron cross-field mobility at 300 V **(b) Electron cross-field mobility at 400 V**

Fig. 24 Mean cross-field electron mobility as a function of harness inductance for the (left) 300 V and (right) 400 V operating conditions. The bars show the RMS oscillation amplitudes.

VIII. Conclusion

This work characterizes discharge voltage, discharge current, cathode-to-ground, thruster body-to-ground, power supply current, and plasma parameter oscillations as a function of harness inductance at two HET operating points. We present when assumptions can be made about the harness, particularly whether it can be treated as a lumped model at low frequencies and as a distributed model at higher frequencies. We also distinguish between ignition and steady-state operation of a HET, where dominant frequencies are high and low, respectively, leading to different harness electrical models that must be used for detailed analysis.

We found that there exists a nonlinear coupling between the harness inductance and oscillatory behavior in a HET through impedance interactions. The link between harness inductance and oscillations stems from the phase shift

introduced by the harness inductance, which alters the timing of the exchange of magnetic energy with the discharge plasma and can thus affect the timing of the breathing mode limit cycle. The RMS of the oscillations exhibit minima and maxima in their characteristic curves as functions of harness inductance. Harness inductance not only affects the electrical dynamics but also affects the plasma dynamics of the HET, changing cathode emission along with thruster body potentials that alter electrical pathways. These findings support the conclusion that while shorter harnesses minimize discharge voltage oscillations, there may exist a different optimal harness length or inductance that can reduce discharge current oscillations. These findings furthermore inform thruster and power system integration strategies by highlighting the role of series inductance in shaping discharge oscillations and pointing toward design approaches such as reactive compensation, power factor correction, and impedance matching for maximum power transfer.

Appendix

Figures 25 and 26 show the unnormalized versions of Figures 22a and 22b:

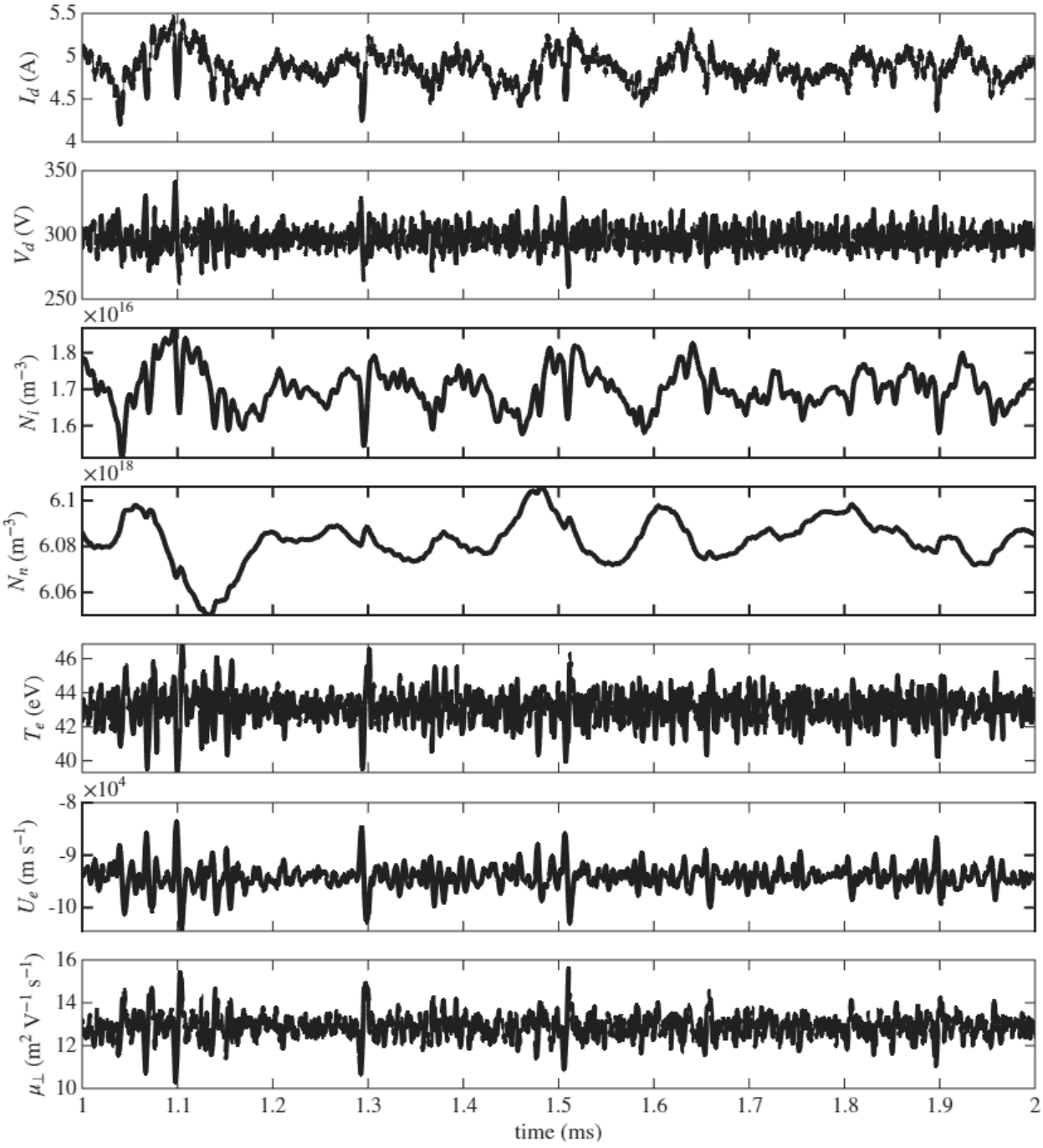


Fig. 25 Unnormalized Plasma Parameters as a Function of Time at 100μH Harness Inductance at 300 V Operating Point

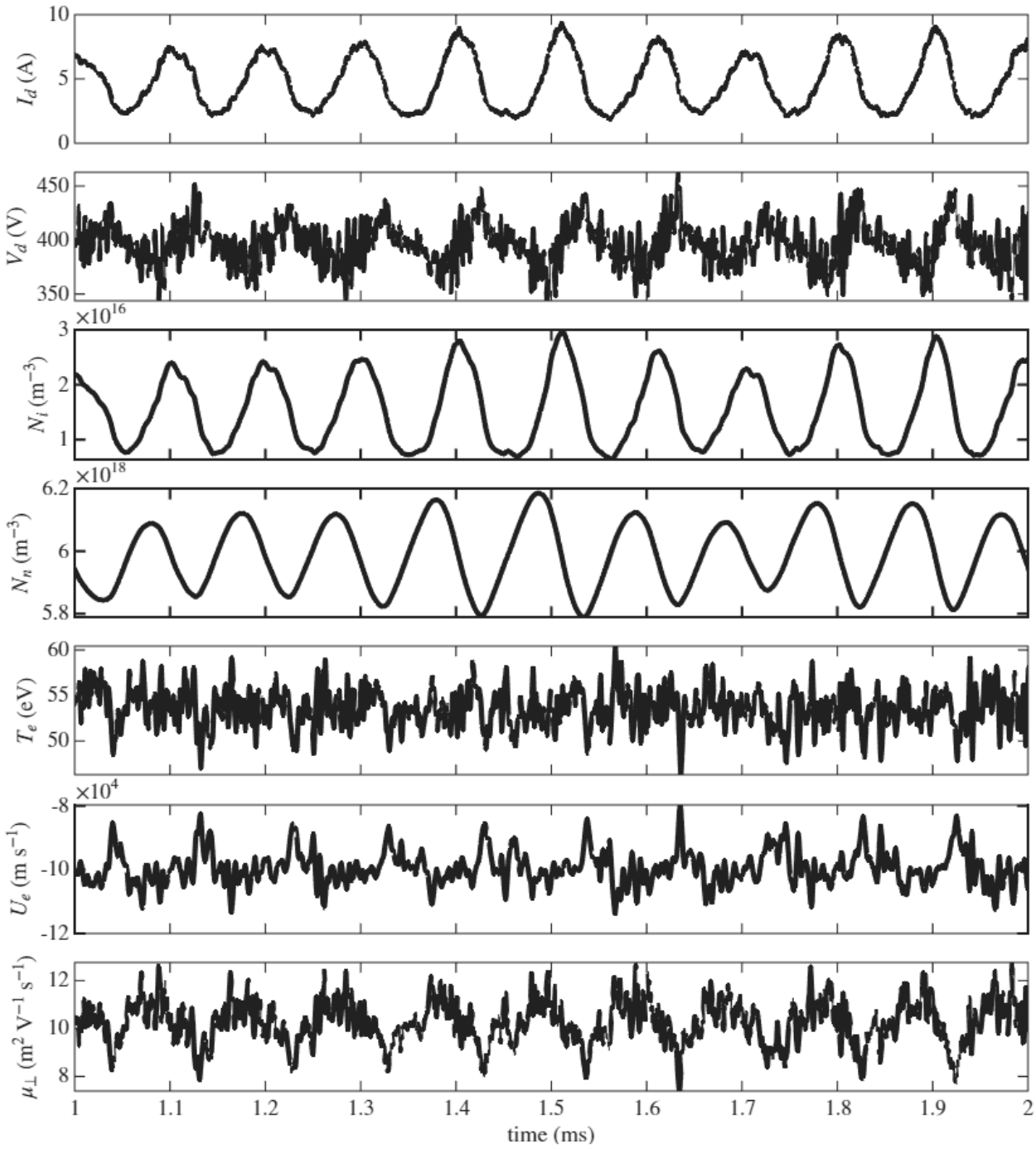


Fig. 26 Unnormalized Plasma Parameters as a Function of Time at 100 μH Harness Inductance at 400 V Operating Point

Figures 27 and 28 show the unnormalized versions of Figures 23a and 23b:

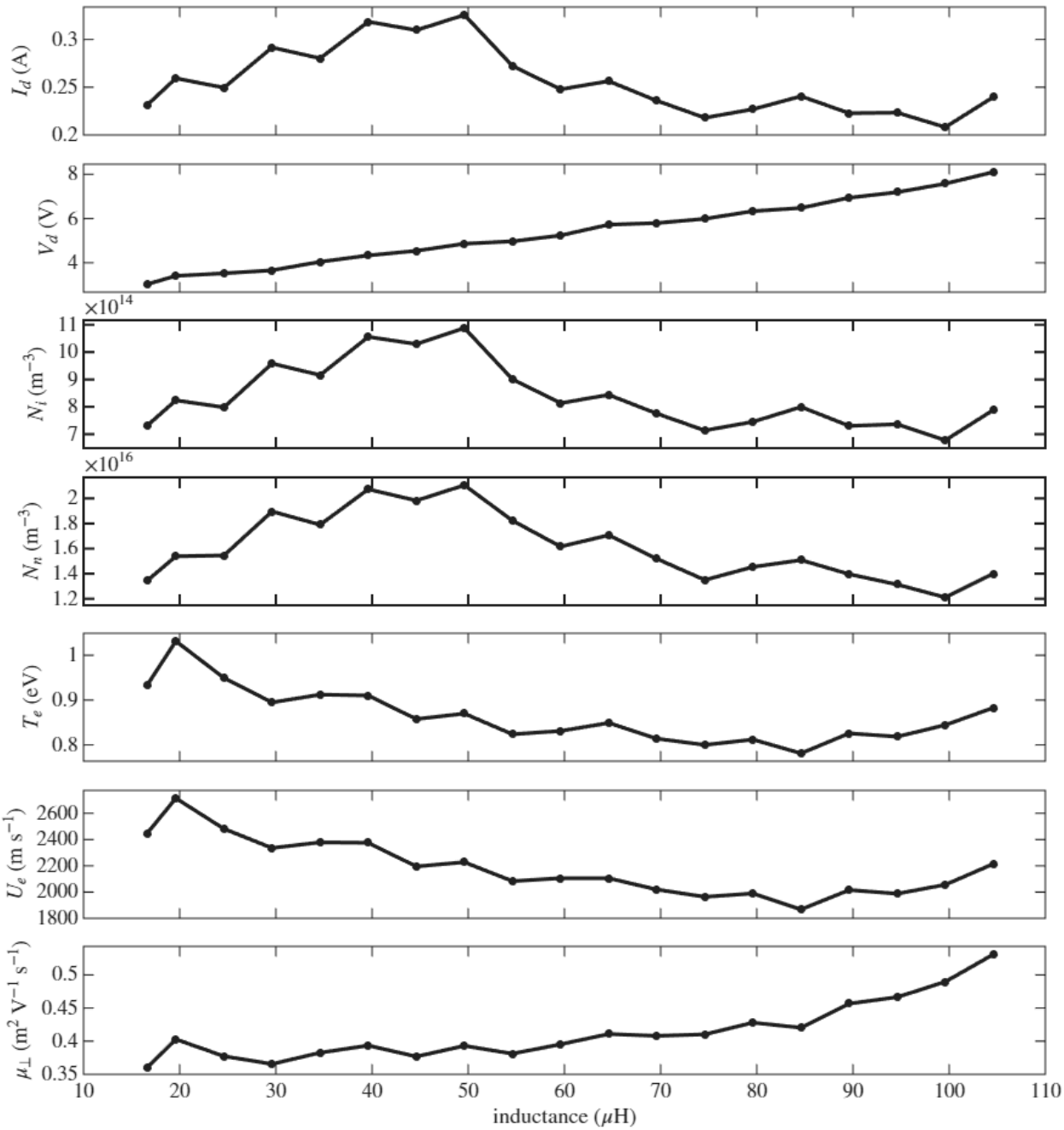


Fig. 27 Unnormalized Plasma Parameters as a Function of Inductance at 300 V Operating Point

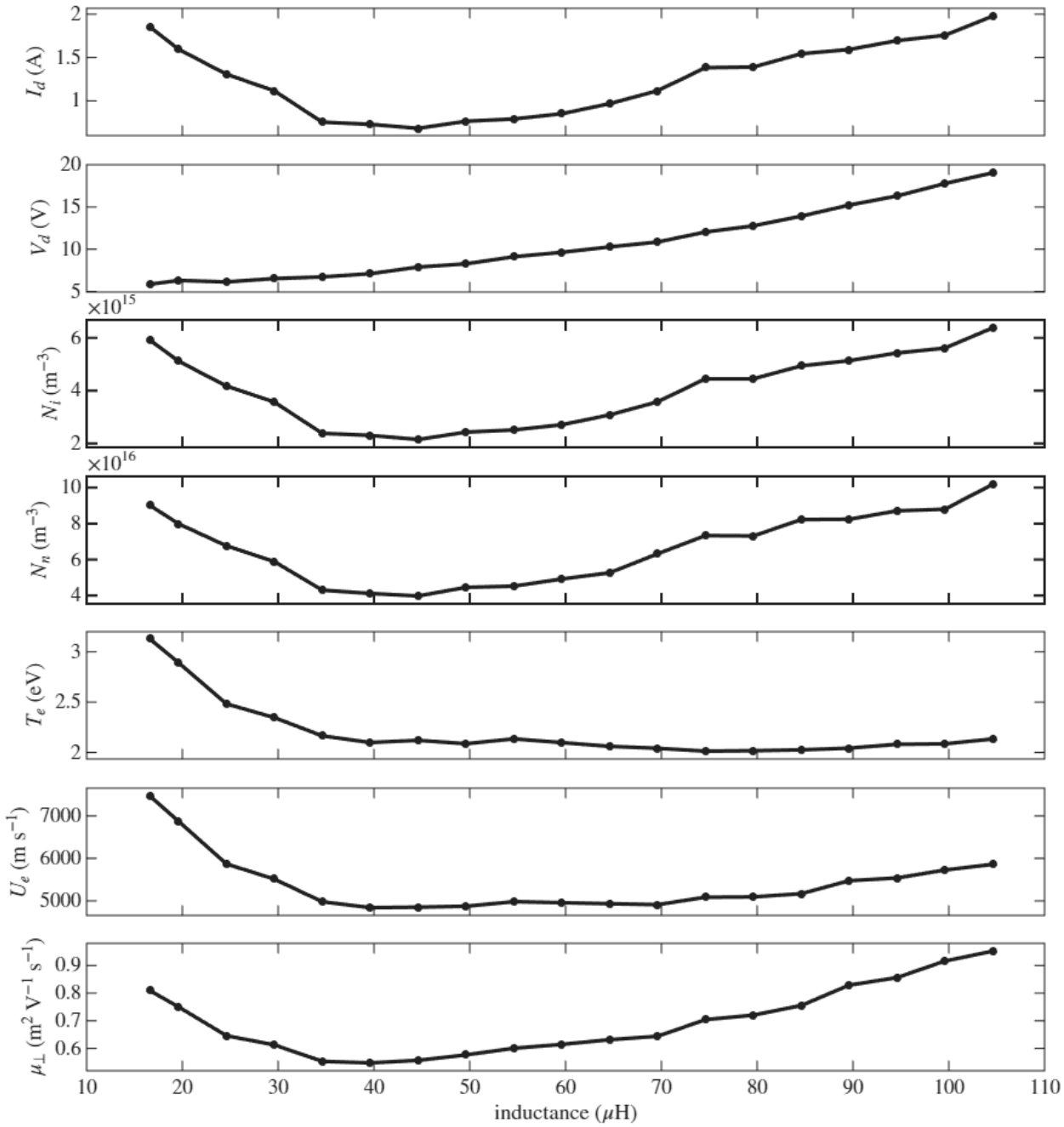


Fig. 28 Unnormalized Plasma Parameters as a Function of Inductance at 400 V Operating Point

Declarations

A. Funding

This work was sponsored by the NASA Joint Advanced Propulsion Institute under the grant number 80NSSC21K1118.

B. Conflicts of Interest/Competing Interests

The authors have no competing interests to declare that are relevant to the content of this article.

C. Data Availability

N/A

D. Code Availability

N/A

E. Author's Contributions

A. Krishnan planned and executed the study, analyzed the data, and wrote the paper. D. Troyetsky and K. Hara developed the plasma parameter and state estimation framework used in the paper and helped with plasma physics analysis. D. Lev and M. Walker also provided guidance on the plasma physics parts of the study. M. Saeedifard provided guidance on the electrical engineering parts of the study.

Acknowledgments

The authors would like to thank all of the undergraduate and graduate student researchers at HPEPL that contributed towards experimental setup and vacuum facility operation, particularly Julian Lopez-Uricoechea, Will Brabston, Nafez Ahmmed, Frank George, Hector Sanchez, Irene Moxley, and Daniel Wochnick. Lastly, the authors would like to thank the NASA Joint Advanced Propulsion Institute for its support under the grant number 80NSSC21K1118.

References

[1] Brown, D. L., "Investigation of low discharge voltage Hall thruster operating modes and ionization processes," *31st International Electric Propulsion Conference*, Ann Arbor, MI, USA, 2009. IEPC-2009-074.

[2] Goebel, D., and Katz, I., *Fundamentals of Electric Propulsion: Ion and Hall Thrusters*, Wiley, Hoboken, NJ, 2008.

[3] Byers, D., "A review of facility effects on Hall effect thrusters," *31st International Electric Propulsion Conference*, Ann Arbor, MI, USA, 2009. IEPC-2009-076.

[4] Frieman, J. D., "Role of a conducting vacuum chamber in the Hall Effect Thruster Electrical Circuit," *Journal of Propulsion and Power*, 2014.

[5] Byrne, M. P., Roberts, P. J., and Jorns, B. A., "Coupling of electrical and pressure facility effects in Hall effect thruster testing," *37th International Electric Propulsion Conference*, Boston, MA, USA, 2022. IEPC-2022-377.

[6] Walker, J. A., "Electrical facility effects on hall current thrusters: Electron termination pathway manipulation," *Journal of Propulsion and Power*, 2016.

[7] Dankanich, J. W., "Recommended practice for pressure measurement and calculation of effective pumping speed in electric propulsion testing," *Journal of Propulsion and Power*, 2017.

[8] Choueiri, E. Y., "Plasma oscillations in hall thrusters," *Physics of Plasmas*, 2001.

[9] Fife, J., Martinez-Sanchez, M., Szabo, J., Fife, J., Martinez-Sanchez, M., and Szabo, J., "A numerical study of low-frequency discharge oscillations in Hall thrusters," *33rd Joint Propulsion Conference and Exhibit*, 1997, p. 3052.

[10] Barral, S., and Ahedo, E., "Theoretical study of the breathing mode in Hall thrusters," *42nd AIAA/ASME/SAE/ASEE Joint Propulsion Conference & Exhibit*, 2006, p. 5172.

[11] Hara, K., Sekerak, M. J., Boyd, I. D., and Gallimore, A. D., "Perturbation analysis of ionization oscillations in Hall effect thrusters," *Physics of Plasmas*, Vol. 21, No. 12, 2014, p. 122103. https://doi.org/10.1063/1.4903843.

[12] Troyetsky, D. E., Greve, C. M., Tsikata, S., and Hara, K., "State estimation for real-time analysis of dynamic plasma properties and electrical circuit effects in Hall effect thrusters," *37th International Electric Propulsion Conference*, Cleveland, OH, USA, 2022. IEPC-2022-323.

[13] Piñero, L. R., "The Impact of Harness Impedance on Hall Thruster Discharge Oscillations," *NASA/TM-2017-219722*, 2017.

[14] Brieda, K. J., L., and Scharfe, M., "Influence of a Power Supply Model on Simulated Hall Thruster Discharge Voltage Oscillations," *AIP Advances*, Vol. 9, No. 2, 2019, pp. 1–5.

[15] Krishnan, A., "Impedance Analysis of the Hall Thruster Discharge Circuit and Plasma Load to Address Harness Facility Effects," *38th International Electric Propulsion Conference*, Toulouse, France, 2024. IEPC-2024-619.

[16] Li, D. Y. W. L. L. H., W., and Yu, D., "Effect of discharge parameters on pulse current during hall thruster start-up," *Elsevier Vacuum*, Vol. 136, 2017, pp. 77–81.

[17] Barral, S., "Numerical investigation of closed-loop control for Hall accelerators," *Journal of Applied Physics*, 2011.

[18] Wei, L., "Stabilizing Low Frequency Oscillation with Two Stages Filter in Hall Thrusters," *34th International Electric Propulsion Conference*, Shanghai, China, 2015. IEPC-2015-284.

[19] Wei, L., "On the frequency characteristic of inductor in the filter of Hall thrusters," *Journal of Vacuum Science and Technology*, 2010.

[20] Wei, L., "Experimental study on the role of a resistor in the filter of Hall thrusters," *Physics of Plasmas*, 2011.

[21] Kieckhafer, A. W., "Recirculating liquid nitrogen system for operation of cryogenic pumps," *32nd International Electric Propulsion Conference*, Kurhaus, Wiesbaden, Germany, 2011. IEPC-2011-217.

[22] Thompson, S. J., Hara, K., Cabrera, J. D., Walker, M. L. R., and Williams, J. D., "Causality Analysis of Vacuum Chamber Facility Effects for Hall Effect Thruster Operation," *Journal of Applied Physics*, 2026. Accepted for publication.

[23] Greve, C. M., Majji, M., and Hara, K., "Real-time state estimation of low-frequency plasma oscillations in Hall effect thrusters," *Physics of Plasmas*, Vol. 28, No. 9, 2021, p. 093509. https://doi.org/10.1063/5.0057751.

[24] Troyetsky, D., Greve, C., Tsikata, S., and Hara, K., "State estimation of the dynamic behavior of plasma properties in a Hall effect thruster discharge," *Journal of Physics D: Applied Physics*, Vol. 56, No. 44, 2023, p. 444001.

[25] Biagi, S. F., "Biagi database v8.97," , 2015. URL www.lxcat.net.

[26] Hobbs, G., and Wesson, J., "Heat flow through a Langmuir sheath in the presence of electron emission," *Plasma Physics*, Vol. 9, No. 1, 1967, p. 85.

[27] Barral, S., Makowski, K., Peradzyński, Z., Gascon, N., and Dudeck, M., "Wall material effects in stationary plasma thrusters. II. Near-wall and in-wall conductivity," *Physics of Plasmas*, Vol. 10, No. 10, 2003, pp. 4137–4152.